

# 1 Long-Term Atmospheric Emissions for the Coal Oil Point 2 Natural Marine Hydrocarbon Seep Field, Offshore California

3 Ira Leifer<sup>1</sup>, Christopher Melton<sup>1</sup>, Donald R. Blake<sup>2</sup>

4 <sup>1</sup>Bubbleology Research International, Solvang, CA 93463, United States

5 <sup>2</sup>University of California, Irvine, Department of Chemistry, Irvine, CA 92697, United States

6 *Correspondence to:* Ira Leifer (Ira.Leifer@bubbleology.com)

7 **Abstract.** In this study, we present a novel approach for assessing nearshore seepage atmospheric emissions through  
8 modeling of air quality station data, specifically, a Gaussian plume inversion model. Three decades of air quality  
9 station meteorology and total hydrocarbon concentration, *THC*, data were analysed to study emissions from the Coal  
10 Oil Point marine seep field offshore California. *THC* in the seep field directions was significantly elevated and  
11 Gaussian with respect to wind direction,  $\theta$ . An inversion model of the seep field,  $\theta$ -resolved anomaly,  $THC'(\theta)$ -derived  
12 atmospheric emissions. The model inversion is for the far field, which was satisfied by gridding the sonar seepage and  
13 treating each grid cell as a separate Gaussian plume. This assumption was validated by offshore *in situ* data that  
14 showed major seep area plumes were Gaussian. Of plume Total Carbon, *TC*, ( $TC=THC$ +carbon dioxide,  $CO_2$ +carbon  
15 monoxide) 18% was  $CO_2$  and 82% was *THC*; 85% of *THC* was  $CH_4$ . These compositions were similar to the seabed  
16 composition, demonstrating efficient vertical plume transport of dissolved seep gases. Air samples also measured  
17 atmospheric alkane plume composition. The inversion model used observed winds and derived the three-decade-  
18 average (1990-2021) field-wide atmospheric emissions of  $83,400 \pm 12,000 \text{ m}^3 \text{ THC d}^{-1}$  ( $27 \text{ Gg THC yr}^{-1}$  based on  $19.6$   
19  $\text{g mole}^{-1}$  for *THC*). Based on a 50:50 air to seawater partitioning, this implies seabed emissions of  $167,000 \text{ m}^3 \text{ THC d}^{-1}$   
20 <sup>1</sup>. Based on atmospheric plume composition,  $C_1$ - $C_6$  alkane emissions were 19, 1.3, 2.5, 2.2, 1.1, and  $0.15 \text{ Gg yr}^{-1}$ ,  
21 respectively. The spatially-averaged  $CH_4$  emissions over the  $\sim 6.3 \text{ km}^2$  of  $25 \times 25 \text{ m}^2$  bins with sonar values above noise,  
22 was  $5.7 \mu\text{M m}^{-2} \text{ s}^{-1}$ . The approach can be extended to derive emissions from other dispersed sources such as landfills,  
23 industrial sites, or terrestrial seepage if source locations are constrained spatially.

Deleted: offshore

Deleted: methane.

Deleted: if

Deleted: were dispersed

Deleted: we find

24

## 25 1 Introduction

### 26 1.1 Seepage and methane

27 On decadal timescales, the important greenhouse gas, methane,  $CH_4$ , affects atmospheric radiative balance far more  
28 strongly than carbon dioxide,  $CO_2$  (IPCC, 2007, Fig. 2.21), yet  $CH_4$  has large uncertainties for many sources (IPCC,  
29 2013) and is very sensitive to hydroxyl (OH) concentration, the primary  $CH_4$  loss mechanism (Y. Zhao et al., 2020).  
30 Since pre-industrial times,  $CH_4$  concentrations have risen by a factor of  $\sim 2.5$ , and after stabilizing in the 1990s and  
31 early 2000s, resumed rapid growth since 2007 (Nisbet et al., 2019). The significantly shorter lifetime of  $CH_4$  than  $CO_2$   
32 argues for  $CH_4$  regulatory priority as emission reductions (and changes to the radiative balance) manifest more quickly  
33 as atmospheric concentrations decrease (Shindell, Faluvegi, Bell, & Schmidt, 2005). Further impetus for a  $CH_4$  focus

Deleted: emissions

40 is a recent estimate that 40% CH<sub>4</sub> emissions reductions are feasible at no net cost for the oil and gas, O&G, industry  
41 (IEA, 2020), a major anthropogenic CH<sub>4</sub> source (IPCC, 2014). This is particularly salient given a recent estimate that  
42 half of recent CH<sub>4</sub> increases are from the O&G industry (Jackson et al., 2020).

43

44 For 2008-2017, global CH<sub>4</sub> top-down emissions estimates are 576 Tg yr<sup>-1</sup>; 1 Tg=10<sup>12</sup> g, range 550-594 Tg yr<sup>-1</sup>, whereas  
45 bottom-up approaches find 737 Tg yr<sup>-1</sup>, range 594-881 Tg yr<sup>-1</sup> (Saunio et al., 2020). A significant fraction of this  
46 discrepancy arises from uncertainty in OH concentration trends and spatial variability (Y. Zhao et al., 2020).  
47 Anthropogenic sources for 2008-2017 were estimated at 336-376 Tg CH<sub>4</sub> yr<sup>-1</sup> based on bottom-up estimates. Natural  
48 sources include wildfires, wetlands, hydrates, and geological seepage. Bottom-up estimates for natural sources are  
49 higher than top-down estimates (Saunio et al., 2020). Geological sources (including seepage) are estimated at 63-80  
50 Tg CH<sub>4</sub> yr<sup>-1</sup> of which marine seepage is estimated to contribute 20-30 Tg CH<sub>4</sub> yr<sup>-1</sup> (Etiopie, Ciotoli, Schwietzke, &  
51 Schoell, 2019) or 5-10 Tg CH<sub>4</sub> yr<sup>-1</sup> (Saunio et al., 2020). For comparison, marine non-geological CH<sub>4</sub> emissions are  
52 estimated at 4-10 Tg yr<sup>-1</sup>. The broad range of this estimate arises from the uncertainty in the fraction of seabed  
53 emissions that reaches the atmosphere and the uncertainty in overall seabed emissions. Further complexity in assessing  
54 geological seepage CH<sub>4</sub> emissions arises because both seepage and O&G emissions source from the same geological  
55 reservoirs (Leifer, 2019) and thus are isotopically similar (Schwietzke et al., 2016).

56

57 Seepage is the process by which petroleum hydrocarbon gases and fluids in the lithosphere migrate to the hydrosphere  
58 and/or atmosphere from a reservoir formation, which underlies a capping layer that seals the formation, allowing  
59 hydrocarbon accumulation. Thus, seepage requires a migration pathway, typically fractures and/or fault networks,  
60 through the capping rock layer(s) (Ciotoli, Procesi, Etiopie, Fracassi, & Ventura, 2020) or where the capping layer has  
61 eroded away, forming an outcropping of the reservoir formation (Abrams, 2005).

62

63 Marine seepage is widespread in every sea and ocean (Judd & Hovland, 2007) and occurs primarily (but not  
64 exclusively) in petroleum systems and mostly in convergent basins (Ciotoli et al., 2020). Quantitative seepage  
65 estimates (for global budgets) are limited (though growing); see Leifer (2019) review and below for more recent.  
66 Fluxes for individual marine seep vents and seep areas have been reported for the Gulf of Mexico (C. Johansen et al.,  
67 2020; Caroline Johansen, Todd, & MacDonald, 2017; Leifer & MacDonald, 2003; Römer et al., 2019; T. C. Weber et  
68 al., 2014), the Black Sea (Greinert, McGinnis, Naudts, Linke, & De Batist, 2010), the southern Baltic Sea (Heyer &  
69 Berger, 2000), various sectors of the North Sea (Borges, Champenois, Gypens, Delille, & Harlay, 2016; Leifer, 2015;  
70 Römer et al., 2017), offshore Norway (Muyakshin & Sauter, 2010; Sauter et al., 2006), offshore Svalbard in the  
71 Norwegian Arctic (Veloso-Alarcón et al., 2019), offshore Pakistan (Römer, Sahling, Pape, Bohrmann, & Spieß, 2012),  
72 offshore the arctic Laptev Sea (Leifer, Chernykh, Shakhova, & Semiletov, 2017), the East Siberian Arctic Sea  
73 (Shakhova et al., 2013), the South China Sea (Di, Feng, Tao, & Chen, 2020), New Zealand's Hikurangi Margin (Higgs  
74 et al., 2019), the Cascadia Margin (Riedel et al., 2018), and the Coal Oil Point (COP) marine hydrocarbon seep field,  
75 hereafter COP seep field, in the northern Santa Barbara Channel, offshore Southern California (Hornafius, Quigley,  
76 & Luyendyk, 1999), and for numerous individual vents in the field (Leifer, 2010).

Deleted: including for geological sources

Deleted: as

79

80 Most seep emission estimates are snapshot values from short-term field campaigns. Seep emissions vary on timescales  
81 from tidal (Leifer & Boles, 2005; Römer, Riedel, Scherwath, Heesemann, & Spence, 2016) to seasonal (Bradley,  
82 Leifer, & Roberts, 2010) to decadal (Fischer, 1978; Leifer, 2019). Additional temporal variability arises from transient  
83 emissions – pulses lasting seconds to minutes (Greinert, 2008; Schmale et al., 2015) to decades (Leifer, 2019). This  
84 shortcoming is being addressed by benthic (seabed) observatories and cabled observatories, e.g., Wiggins, Leifer,  
85 Linke, and Hildebrand (2015); Greinert (2008), Kasaya et al. (2009); Römer et al. (2016); Scherwath et al. (2019).  
86 Still, benthic observatories are costly and thus uncommon.

87

88 Seepage contributes to oceanographic budgets and to a lesser extent, to atmospheric budgets due to water-column  
89 losses with significant uncertainty in the partitioning. As a result, uncertainty in the atmospheric contribution is much  
90 larger than the (significant) uncertainty in seabed emissions. Seepage partitioning between the atmosphere and ocean  
91 - where microbial degradation occurs on timescales inversely related to concentration (Reeburgh et al., 1991) -  
92 depends primarily on depth (Leifer & Patro, 2002) with little to none of deepsea seabed emissions reaching the  
93 atmosphere, e.g., Römer et al. (2019). In contrast, very shallow seepage (meter scale) largely entirely reaches the  
94 atmosphere both by direct bubble-mediated transfer and diffusive transport. For intermediate depths, the  
95 ocean/atmospheric partitioning is complex and depends on depth, bubble flux, bubble size distribution, bubble  
96 interfacial conditions, and other characteristics (Leifer & Patro, 2002). Whereas the indirect diffusive flux (proximate  
97 and distal) depends on bubble dissolution depth (Leifer & Patro, 2002), vertical turbulence transport in the winter  
98 wave-mixed layer (Rehder, Keir, Suess, & Rhein, 1999), microbial oxidation losses, and exchange through the sea-  
99 air interface.

100

101 A range of approaches have been used to estimate the sea-air flux. The most common is by measuring the atmospheric  
102 and water concentrations and applying air-sea gas exchange theory for the measured wind speeds, e.g., Schmale,  
103 Greinert, and Rehder (2005) for Black Sea seepage under weak wind speeds. Sea-air exchange is a diffusive turbulence  
104 transfer process that depends on the air-sea concentration difference and the piston velocity,  $k_T$ , which depends on gas  
105 physical properties, wind speed,  $u$  (Liss & Duce, 2005), wave development (D. Zhao, Toba, Suzuki, & Komori, 2003)  
106 including wave breaking (Liss & Merlivat, 1986), and surfactant layers at low wind speeds that suppress gas exchange  
107 (Frew et al., 2004).  $k_T$  increases rapidly and non-linearly with  $u$  and has been parameterized by piecewise linear  
108 functions (Wanninkhof, Asher, Ho, Sweeney, & McGillis, 2009) or by a cubic function (Nightingale et al., 2000). Air-  
109 sea gas exchange theory is for (relatively) homogeneous atmospheric and oceanographic fields (concentrations, winds,  
110 and wave development), and thus is inappropriate for point-source (bubble-plume) emissions and for the near-field  
111 downcurrent plume, which tends to be heterogeneous.

112

113 Another approach uses seabed bubble size measurements or an assumed bubble size distribution to initialize a  
114 numerical bubble propagation model to predict direct bubble-mediated atmospheric fluxes (Leifer et al., 2017; Römer  
115 et al., 2017; Schneider von Deimling et al., 2011). The dissolved portion that evades to the atmosphere could be

Deleted: water

Deleted: ,

118 addressed by a dispersive model coupled to an air-sea gas exchange model, though studies have not yet addressed this  
119 component.

120

121 An alternate approach is to derive atmospheric emissions by plume inversion. Leifer, Luyendyk, Boles, and Clark  
122 (2006) derived emissions for a blowout from Shane Seep in the COP seep field by a plume inversion. This neglected  
123 the portion that dissolves during bubble rise and drifts downcurrent, out of the bubble plume's vicinity before sea-air  
124 gas transfer into the atmosphere. Note dissolved gas evasion in the plume vicinity contributes to the inversion  
125 emissions estimate.

126

### 127 1.2 Study motivation

128 In this study, we present a novel approach for assessing nearshore seepage atmospheric emissions – air quality station  
129 data modeling, specifically using a Gaussian plume inversion model. This model requires that source locations are  
130 mapped, spatially stable, and lie within a fairly constrained distance range band. These conditions are met for the COP  
131 seep field, ~~located~~ near the West Campus air quality Station (WCS). ~~The~~ COP seep field lies in ~~the~~ shallow coastal  
132 waters of northern Santa Barbara Channel, CA. Spatial constraint is provided by geological structures, such as faults,  
133 that constrain emission locations. The Gaussian plume model assumes a far-field source, whereas WCS is in the  
134 nearfield of the extensive COP seep field. To satisfy the far field criterion, the source was gridded and each grid cell's  
135 emissions treated as a distinct (distant) Gaussian plume. This characterization was validated in an offshore survey of  
136 several focused COP seep field seepage areas, ~~whose atmospheric plumes~~ were well-modeled as Gaussian,

137

138 Thus, this study demonstrates an approach to deriving emissions from air quality station data for an area source such  
139 as ~~a~~ natural marine seep ~~field~~. This approach could be used to derive emissions from other dispersed sources such as  
140 landfills, industrial sites, or natural terrestrial seepage where ~~source~~ locations are constrained spatially.

141

### 142 1.3 Water column marine seabed seepage fate

143 Seep seabed CH<sub>4</sub> partitioning between the atmosphere and water column depends on seabed depth and emission  
144 character – as bubbles, bubble plumes (Leifer & Patro, 2002), or dissolved CH<sub>4</sub>. Dissolved CH<sub>4</sub> migration through the  
145 sediment is oxidized largely by near-seabed microbes (Reeburgh, 2007), termed the microbial filter, negating its  
146 contribution ~~and~~ leaving only bubble-mediated ~~migration~~.

147

148 As seep bubbles rise, they dissolve, losing gas to the surrounding water at a rate that decreases with time. Smaller and  
149 more soluble gases dissolve faster than larger and less soluble gases, i.e., fractionation (Leifer & Patro, 2002).  
150 Additionally, larger bubbles transport their contents upwards more efficiently than smaller bubbles (Leifer et al.,  
151 2006). Sufficiently large bubbles reach the sea surface with a significant fraction of their seabed CH<sub>4</sub> from depths of  
152 even hundreds of meters (Solomon, Kastner, MacDonald, & Leifer, 2009). There are synergies, too with higher plume

Deleted: which

Deleted: is

Deleted: which

Deleted: plumes

Deleted: age

Deleted: the

Deleted:

Deleted: ,

Deleted: flow

162 fluxes driving a stronger upwelling flow that transports plume fluids with dissolved gases upwards towards the sea  
163 surface where air-sea gas exchange drives evasion (Leifer, Jeuthe, Gjosund, & Johansen, 2009). Another synergy  
164 arises from the elevated dissolved plume CH<sub>4</sub> concentration (Leifer, 2010; Leifer et al., 2006), which slows  
165 dissolution. Also, most bubbles are oil-coated (Leifer, 2010), which slows dissolution.

166  
167 Moreover, gases in bubbles that dissolve in the wave-mixed layer (or reach it by the upwelling flow) then diffuse to  
168 the sea surface due to wave and wind turbulence and then evade. Note, microbial degradation removes a portion of  
169 the dissolved CH<sub>4</sub>, which therefore never reaches the air-sea interface. Thus, there are two timescales that govern the  
170 fraction that evades – the microbial degradation timescale, which increases as concentrations decrease, and the  
171 diffusion timescale, which decreases with increasing wind speed. As a result, there is a dissolved plume that drifts  
172 downcurrent, with evasion from this drifting plume creating a linear-source atmospheric plume. Note, dissolved plume  
173 concentrations slowly decrease with time (downcurrent distance) from sea-air gas exchange losses, microbial  
174 oxidation, and dispersion, leading to a decreased atmospheric plume.

#### 176 1.4 Atmospheric Gaussian plumes

177 Strong, focused atmospheric plumes are created from the bursting of seep plume bubbles at the sea surface and from  
178 dissolved gas evasion within the bubble surfacing footprint. This evasion is enhanced by water-side turbulence from  
179 rising and bursting bubbles (Leifer et al., 2015). Atmospheric plume evolution is described by the Gaussian plume  
180 model (Hanna, Briggs, & Hosker Jr., 1982), which relates downwind concentrations to wind transport and turbulence  
181 dispersion and is the basis of the inversion calculation (see Supp. Sec. S1 for details).

#### 183 1.5 Setting

##### 184 1.5.1 The Coal Oil Point seep field

185 The COP seep field (Fig. 1) is one of the largest seep fields in the world, with estimated 1995-1996 seabed total  
186 hydrocarbon, *THC*, emissions,  $E_B$ , of  $1.5 \times 10^5 \pm 2 \times 10^4 \text{ m}^3 \text{ d}^{-1}$  (Hornafius et al., 1999). Hereafter emissions and  
187 concentrations are for *THC* unless noted. Clark, Washburn, Hornafius, and Luyendyk (2000) estimated that half of  
188 the COP seep field  $E_B$  reach the atmosphere in the near field. This is due to shallowness, bubble oiliness, high plume  
189 bubble densities, and turbulence mixing within the wave-mixed layer.

191 Geological structures play a critical role in the spatial distribution of seepage (Leifer, Kamerling, Luyendyk, & Wilson,  
192 2010), which lies along several trends in waters from a few meters to ~85 m deep. These trends follow geologic  
193 structures including anticlines, synclines, and faults in the reservoir formation, the Monterey Formation and overlying  
194 Sisquoc Formation. Faults and fractures associated with damage zones provide migration pathways with seepage  
195 scattered non-uniformly along the trends, including focused seep areas that are highly active, localized, and often are  
196 associated with crossing faults and fractures (Leifer et al., 2010). Seepage in these areas typically surrounds a focus

Deleted: air-

Deleted: interface

Deleted: bursting

Deleted: wave

201 and decreases with distance, primarily along linear trends (Leifer, Boles, Luyendyk, & Clark, 2004). See Supp. Table  
202 S3 for informal names and locations of selected focused seep areas.

203

### 204 1.5.2 Coal Oil Point seep field emissions and composition

205 COP seep field sources from the South Ellwood oil field whose primary source rock is Monterey Formation, which is  
206 immature to marginally mature. Petroleum gases from marine organic materials have relatively higher proportion of  
207 ethane, propane, butane, etc., relative to ~~CH<sub>4</sub>~~ as compared to petroleum gases from terrestrial organic materials. The  
208 wet gas fraction (C<sub>2</sub>-C<sub>5</sub>/C<sub>1</sub>-C<sub>5</sub>) indicates a thermogenic origin of greater than 0.05 (Abrams, 2017). Of the saturated  
209 alkanes, the alkenes (olefins) are of biological origin. Additionally, the ethane/ethene ratio and propane/propene ratios  
210 can be indicators of seep gas biogenic modification with values above 1000 indicating purely thermogenic origin  
211 (Abrams, 2017; Bernard, Brooks, & Zumberge, 2001).

212

213 In this study, we analyse WCS (located at 34° 24.897'N, 119° 52.770'W) atmospheric ~~THC and wind data~~. Clark,  
214 Washburn, and Schwager (2010) report average seep field seabed [bubble gas fractions](#) of CH<sub>4</sub>, CO<sub>2</sub>, and non-methane  
215 hydrocarbons (NMHC), of 76.7, 15.3, and 7.7%, respectively, with Trilogy Seep seabed compositions of 67, 21, and  
216 7.8%, respectively. With respect to alkanes, seabed bubbles are 90.4% CH<sub>4</sub> and 8.6% NMHC. CO<sub>2</sub> rapidly escapes  
217 the bubbles and is negligible (<1%) at the sea surface. At the sea surface, CH<sub>4</sub> in bubbles is ~90% with NMHC making  
218 up the remaining 10%, neglecting air gases (Clark et al., 2010). Note, whereas seep *THC* is predominantly CH<sub>4</sub>, *THC*  
219 from terrestrial directions [is composed predominantly of](#) NMHC from traffic and other anthropogenic sources as well  
220 as CH<sub>4</sub> from pipeline leaks, terrestrial seeps, etc.

221

### 222 1.5.3 Northern Santa Barbara Channel climate

223 Diurnal and seasonal wind cycles are important to the atmospheric transport of COP seep field emissions. The Santa  
224 Barbara climate is Mediterranean with a dry season and a wet seasons when storms occur infrequently (Dorman &  
225 Winant, 2000). The semi-permanent eastern Pacific high-pressure system plays a dominant controlling role in weather  
226 in the Santa Barbara coastal plain. This high-pressure system drives light winds and strong temperature inversions that  
227 act as a lid that restricts convective mixing to lower altitudes. The coastal California boundary layer is shallow, from  
228 0 to 800 m thick (Edinger, 1959); generally 240-300 m around Santa Barbara (Dorman & Winant, 2000). Additionally,  
229 coastal mountains provide physical barriers to transport (Lu, Turco, & Jacobson, 1997).

230

231 As a coastal environment, the land/sea breeze is important to overall wind-flow patterns with weak offshore night  
232 winds and stronger onshore afternoon winds (Dorman & Winant, 2000). In coastal Santa Barbara, warming on [the](#)  
233 mountaintops [\(and more interior arid lands\)](#) relative to [the](#) cooler marine temperatures drives the sea breeze.  
234 Downslope nocturnal flows warm nocturnal surface temperatures, moderating the coastal diurnal temperature cycle  
235 (Hughes, Hall, & Fovell, 2007).

Deleted: methane

Formatted: Subscript

Deleted: .

Deleted: arises from

239

240 Typical morning winds are calm, offshore, and often accompanied by a cloud-filled marine boundary layer, 50–150  
241 m thick (Lu et al., 1997). The marine layer usually (but not always) “burns off” by mid-morning, after which  
242 temperatures rise, the boundary layer thickens, and winds shift clockwise from offshore to prevailing westerlies  
243 aligned with the coastal mountains. Midday through late afternoon and even evening, winds strengthen, often leading  
244 to whitecapping before the boundary layer collapses and winds return to the nocturnal pattern.  
245

Deleted: and

Deleted: eventually

## 246 2 Methods

### 247 2.1 West Campus Station data

248 WCS data includes wind speed,  $u$ , and direction,  $\theta$  by a vane anemometer (010C,020C, Met One, Grants Pass, OR)  
249 and  $THC$  concentration,  $C$ , by a Flame Ionization Detector (51i-LT, Thermo Scientific, MA). WCS is maintained by  
250 the Santa Barbara County Air Pollution Control District. Daily instrument calibration occurs after midnight, rendering  
251  $C$  unavailable 00:50 to 02:09 local time, LT. WCS was improved significantly in 2008 from 1-hour to 1-minute time  
252 resolution, which allowed far higher values of  $C$  and  $u$  due to the shorter averaging times. Data analysis uses custom  
253 routines as well as standard routines and functions in MATLAB (MathWorks, MA).  
254

255 First, WCS data were quality controlled to remove all values of  $C$  during the daily calibration, as well as to interpolate  
256 neighboring values that were unrealistically low, i.e.,  $C$  less than 1.6 ppm in the 1990s and 1.85 ppm in the 2000s.  
257 Data since 2008 were smoothed by nearest-neighbor averaging, yielding 3-minute time resolution. Data prior to 2008  
258 were hourly and were not smoothed. Wind data were nearest-neighbor averaged after decomposing into north and east  
259 components, followed by recalculation of  $u$  and  $\theta$ .  
260

### 261 2.2 *In situ* marine surveys

262 Offshore *in situ* survey data were collected by the *F/V Double Bogey*, a 12-m, 9-ton, fishing vessel with a near  
263 waterline deck ( $\sim 0.2$  m) and low overall profile (cabin at  $\sim 2.2$  m). A sonic anemometer (VMT700, Vaisala) was  
264 mounted on a 6.5-m tall, 5-cm (2”) diameter aluminum mast and measured 3D winds. Continuous  $CH_4$  and  $CO_2$  data  
265 were collected at 5 Hz by a Cavity Enhanced Absorption Spectroscopy (CEAS) analyzer (FGGA, LGR Inc., San Jose,  
266 CA). Vessel location and time were from a Global Positioning System (GPS) at 1 Hz (19VX HVS, Garmin, KS).  $CH_4$   
267 and  $CO_2$  calibration with a greenhouse gas air calibration standard ( $CH_4$ : 1.981 ppmv;  $CO_2$ : 404 ppmv, Scott Marin,  
268 CA, purchased 2015, Sigma Aldrich, St Louis, MO).  
269

Deleted: ,

270 Data are real-time integrated and visualized in Google Earth on a portable computer (Spectre360, HP) using custom  
271 software, written in MATLAB (MathWorks, MA) that is described elsewhere (Leifer, Melton, Fischer, et al., 2018;  
272 Leifer, Melton, Manish, & Leen, 2014; Leifer, Melton, Tratt, et al., 2018; Leifer et al., 2016). Real-time visualization

Deleted: real

277 facilitates adaptive surveys, wherein the survey route is modified based on real-time data to improve outcomes  
278 (Thompson et al., 2015) - in this case to facilitate plume tracking and to ensure transects were near orthogonal to the  
279 wind.

280  
281 Accurate, absolute winds are calculated from relative winds after accounting for vessel motion and filtering for non-  
282 physical velocity changes due to GPS uncertainty (Leifer, Melton, Fischer, et al., 2018). Filtering removes transient  
283 winds that are not relevant to plume transport. The filter interpolates GPS positions flagged as unrealistic.

284  
285 Whole air samples were collected in evacuated 2-liter stainless steel canisters, which were filled gently over ~1 minute  
286 from ~1 m above the sea surface. The filled canisters were analysed in the Rowland/Blake Laboratory at the University  
287 of California, Irvine for carbon monoxide, CO, CH<sub>4</sub>, and C<sub>2</sub>-C<sub>7</sub> organic compounds. Samples were analysed by a gas  
288 chromatography multi-column/detector analytical system utilizing flame ionization detection.

Deleted: analyzed

Deleted: laboratory

### 290 2.3 Seep plume emissions model

291 The plume inversion model is a three-step process (Leifer, Melton, Fischer, et al., 2018; Leifer, Melton, Tratt, et al.,  
292 2018; Leifer et al., 2016). Emissions from focused seep areas were derived from offshore data by first fitting Gaussian  
293 function(s) to orthogonal transect  $C'$  data, termed the data model.  $C'$  is relative to  $C$  outside the plume, derived by  
294 linear interpolation across the plume transect. The data model is derived by error minimization using a least-squares  
295 linear-regression analysis (Curve fitting toolbox, MathWorks, MA). Next, the Gaussian plume model (Eqn. S1; Supp.  
296 Figs. S1 and S2) is fit to the data model. Transect data are collected close to orthogonal to the wind direction and are  
297 projected in the wind direction onto an orthogonal plane. See Leifer, Melton, Tratt, et al. (2018) for a validation study  
298 of the plume inversion model by comparison with remote sensing-derived emissions (which are largely insensitive to  
299 transport). The study found *in situ* and remote-sensing derived emissions agreed within 11%.

### 301 2.4 Seep field emissions model

302 The inversion model was written in MATLAB (MathWorks, MA) and is based on gridding the seep field into  
303 numerous, small additive Gaussian plumes that represent the area emissions. This assumes that each sea-surface grid  
304 cell contributes a Gaussian plume, an assumption that was tested during an offshore survey that collected meteorology  
305 and *in situ* concentration data downwind of several active seep areas.

Deleted: and was written in MATLAB (MathWorks, MA)

306  
307 The definition of an area source versus a point source depends on the relevant distance scales – an area source is well  
308 approximated as a point-source plume if sufficiently downwind (far field), where the distance for “sufficiently  
309 downwind” depends on the area source’s dimensions and meteorological conditions. Whereas WCS is near field for  
310 the entire seep field plume, it is far field for the small plumes from each grid cell.

Deleted: length



316 The area source was based on a Sept. 2005 sonar return,  $\omega$ , map (Fig. 1), see Leifer et al. (2010) for sonar survey  
317 details; data were re-analysed for this study. Simulations used sonar data gridded at a hybrid 22/56-m in a UTM  
318 coordinate system, with the origin at WCS. Specifically, gaps in the 22-m map were filled from the 56-m map (Supp.  
319 Fig. S3). The probability distribution of  $\omega$  was used to identify the noise level (Supp. Fig. S4), as in Leifer et al. (2010).  
320

321 The model calculates a Gaussian plume for  $E_{i,j}$  for grid cell  $i$  and  $j$ , for each grid cell with  $\omega$  above noise.  $C'_{sim}(x, y)_{i,j}$   
322 and for the observed wind-direction,  $\theta$ , resolved wind,  $u(\theta)$ , for a typical Santa Barbara channel boundary layer,  
323  $BL=250$  m. The initial  $E_{i,j}$  was calculated by scaling such that the integrated sonar return,  $\int \omega(x, y)$ , scales to  
324  $E_A=1.5 \times 10^5 \text{ m}^3 \text{ dy}^{-1}$ , i.e.,  $E_B$  from Hornafius et al. (1999). The Gaussian plume is calculated in a Cartesian coordinate  
325 system (Supp. Fig. S5A), rotated to  $\theta$ , and then interpolated linearly to double the spatial resolution. Next, the rotated  
326 plume is regridded to UTM coordinates using the `fgrid.m` function (Supp. Fig. S5B). Interpolation removes gaps in  
327 the regridded plume map. Then, the regridded plume is renormalized to ensure total mass is conserved before and  
328 after these operations. Rotated regridded plumes are translated to the seep field grid and added, yielding  $C'_{sim}(x, y)$ ,  
329 which is the simulated seep field plume anomaly (Supp. Fig. S5C).  
330

331 The model scans  $\theta$  for the seep directions ( $110^\circ < \theta < 330^\circ$ ) and calculates the simulated plume anomaly,  $C'_{sim}(\theta)$  at  
332 WCS, which is compared with the observed WCS concentration,  $C'_{obs}(\theta)$ . Hereafter,  $C_{obs}$  and  $C_{sim}$  and their  
333 anomalies refer to values at WCS.  $C'_{obs}(\theta)$  is defined,

$$334 \quad C'_{obs}(\theta) = C_{obs}(\theta) - \min(C_{obs}(\theta)) \quad (1)$$

335 with the minimum typically from the west in a direction with no known seepage. Specifically,  $C'_{obs}(\theta)$  was calculated  
336 by subtracting the minimum in the annualized observed  $C_{obs}(t, \theta)$  each year,  $t$ , after applying a 7-year running  
337 average.  
338

339 Emissions from suburban communities, light industry, and commercial centers enhance  $C'_{obs}(\theta)$  for the northwest to  
340 northeast ( $\sim 330$ - $30^\circ$ ). These terrestrial emissions were removed by fitting a Gaussian function to  $C'_{obs}(\theta)$  for  
341  $330^\circ < \theta < 30^\circ$  with the residual yielding  $C'_{obs}(\theta)$ . This only affected  $C'_{obs}(\theta)$  for overlapping directions corresponding  
342 to the seep fields' eastern edge.  
343

344 Simulations were run at angular resolutions of  $2^\circ$ . Higher angular resolution produced small artifacts for the 22/56-m  
345 sonar grid while the 11-m sonar grid was overly sparse due to the distance between sonar tracks (Supp. Fig. S3A).  
346

347 The source is the  $\omega$  map in units of decibels, whereas emissions are in units of moles  $\text{m}^{-2} \text{ s}^{-2}$ . Given that the relationship  
348 between  $\omega$  and bubble density (emissions) is complex and non-linear (Leifer et al., 2017), there is poor agreement  
349 between  $C'_{sim}(\theta)$  and  $C'_{obs}(\theta)$ . Thus, a correction function,  $K(\theta)$ , is applied to emissions for each grid cell along each  
350  $\theta$ ,  $E_{i,j}(\theta)$ , and the model is rerun.  $K(\theta)$  is defined,

Deleted: sonar survey

Deleted: ,

Deleted: Then

354 
$$K(\theta) = C'_{obs}(\theta) / C'_{sim}(\theta). \quad (2)$$

355 Initially,  $K(\theta) = 1$ , which is scaled as in Eqn. 2 in subsequent iterations. Because  $K(\theta)$  weights closer seeps more than  
 356 more distant seeps, a distance-varying correction function,  $K(r, \theta)$ , was calculated such that,

357 
$$\int_{r=0}^{r=\infty} E_A(r, \theta) = \int_{r=0}^{r=\infty} K(r, \theta) E_A(r, \theta) dr \quad (3)$$

358 where  $r$  is distance from WCS.  $E_A$  from simulations for different northwards shifts of WCS were fit with a polynomial  
 359 to derive the function form of  $K(r)$ . Accounting for off-axis plume contributions requires several iterations to achieve  
 360 Convergence, which was defined,

361 
$$Convergence = \frac{\sum C'_{sim}(\theta) \sum C'_{obs}(\theta)}{\sum C'_{obs}(\theta)}. \quad (4)$$

362 Iterations continued to Convergence of 1% or better – typically 4 to 5 iterations. Simulations suggest wind veering,  
 363  $\psi$ , was important, which was implemented by calculating  $C'(\theta)$  and assigning it to  $C'(\theta + \psi)$ .

364

### 365 3 Results

#### 366 3.1 Offshore *in situ* surveys

367 An offshore COP seep field survey measured *in situ*  $C_{CH_4}$  and  $u$  on 28 May 2016. Data were collected from the Santa  
 368 Barbara harbor (~7.5 km east of the seep field, Fig. 2A; Supp. Fig. S6) to offshore Naples, several kilometers west of  
 369 the seep field. Overall winds were easterly with an onshore component near Campus Point flowing onto UCSB and a  
 370 broad (6-km wide) offshore flow west of COP that shifts to along coast near Naples (Fig. 2A, white arrows). Observed  
 371 winds veered ~10° from the east to west sides of the seep field, roughly comparable to the shift in coastline orientation.

372

373 Plumes are apparent downwind of major seeps, with the largest plume associated with the Trilogy Seep (Fig 2B).  
 374 Strong plumes also are evident downwind of the La Goleta Seep and Patch Seep. Notably, the Seep Tent Seep plume  
 375 was very weak. The Seep Tent Seep was the dominant seep area in the COP seep field from its appearance in June  
 376 1973 (Boles, Clark, Leifer, & Washburn, 2001) until recent years.

377

378 Additionally, the offshore survey identified focused plumes from beyond the extent of the seep field's 2005-sonar  
 379 map. Specifically in the Goleta Bay, which has been noted (Jordan et al., 2020), and offshore Haskell and Sands  
 380 Beaches, an area with abandoned oil wells, and off Naples Point (Fig. 2A, red arrow).

381

382 Plume alkane  $C'$  were determined by the difference between two “background” air samples collected immediately  
 383 outside the plume and three Trilogy Seep plume air samples.  $CH_4$  was 88.5% of  $THC$ , with ethane, propane, and  
 384 butane at 3.1%, 4.2%, and 2.8%, respectively, with pentane, hexane, and heptane at 1.11, 0.13, and 0.04%, respectively  
 385 (Table 1). Mean  $THC$  molecular weight is 19.6 g mole<sup>-1</sup> based on a composition weighting. Branched alkanes were

Deleted: but in subsequent iterations,  $K(\theta)$

Deleted: the

388 detected, with 2-methylpentane and 3-methylpentane comprising 0.21%, each, as well as simple aromatics, e.g.,  
389 benzene and toluene, with concentrations of 78 and 18 ppm, respectively.

390

391 The observed wet gas fraction,  $\sum_{n=2}^5 C_n / \sum_{n=1}^5 C_n$  was 0.11 indicating a thermogenic origin, i.e., greater than 0.05  
392 (Abrams, 2017) - and thus derived from marine organic materials. Although the olefins ethene and ethyne were  
393 detectable at 0.02% and 0.004%, respectively, butene was not detected. These olefins primarily derive from microbial  
394 processes (Abrams, 2017), thus, the ethane/ethyne ratio of 6200 strongly indicates a thermogenic source (Bernard et  
395 al., 2001). Plume atmospheric CO<sub>2</sub> was elevated by 12 ppm, thus CO<sub>2</sub> was 18% of Total Carbon, *TC*, - defined *TC* =  
396 *THC*+CO<sub>2</sub>+carbon monoxide, CO. CO was elevated minimally in the plume, by just 2 ppb. Given that CO<sub>2</sub> completely  
397 dissolves from bubbles well before reaching the sea surface (Clark et al., 2010), this demonstrates efficient vertical  
398 transport of dissolved seep gases to the sea surface.

399

400 Plumes for the Trilogy Seeps, La Goleta Seep, and Seep Tent Seep were inverse Gaussian plume modeled to derive  
401 emissions for each plume. For the Trilogy Seeps, the average *u* across the plume was 5.9 m s<sup>-1</sup>, insolation was full  
402 sun, and the source height was set at 25 m based on Trilogy's atmospheric plume being buoyant. Plume model surface  
403 concentrations for Trilogy B plume are shown in Fig 2B. The other two seeps are far less intense and used a 1-m  
404 source height.

405

406 *E* for Trilogy A was 1.28 Gg CH<sub>4</sub> yr<sup>-1</sup> (5600 m<sup>3</sup> CH<sub>4</sub> d<sup>-1</sup>), whereas Trilogy B and C contributed 0.06 and 0.07 Gg CH<sub>4</sub>  
407 yr<sup>-1</sup>, respectively, for a total of 6200 m<sup>3</sup> CH<sub>4</sub> d<sup>-1</sup>. Note, plume origins and the sonar seep bubble plume locations do not  
408 precisely match because the sonar map is for near the seabed, and currents deflect the bubble surfacing location, up to  
409 ~40 m. La Goleta Seep released 4000 m<sup>3</sup> CH<sub>4</sub> d<sup>-1</sup> and the Seep Tent Seep released 310 m<sup>3</sup> CH<sub>4</sub> d<sup>-1</sup> with almost no  
410 surface bubble expression. For comparison, Clark et al. (2010) used a flux buoy, which measures near surface bubble  
411 fluxes, and found Trilogy Seep emissions of 5500 and 4200 m<sup>3</sup> THC d<sup>-1</sup> and 930 m<sup>3</sup> THC d<sup>-1</sup> for La Goleta Seep in  
412 2005 and 5700 m<sup>3</sup> THC d<sup>-1</sup> for the Seep Tent Seep in 2002. During the cruise, surface bubble plumes were not observed  
413 for the Seep Tent Seep, although its bubble plume had been a perennial and dominant feature since its appearance.

414 For reference, Clark et al. (2010) reported *THC* in near sea surface bubbles was 91% CH<sub>4</sub>.

415

## 416 3.2 West Campus Station

### 417 3.2.1 Temporal trends

418 WCS is 500 m from the coast (to the southwest), at 11-m altitude, and 850 m almost due south of the ~11-m altitude  
419 bluffs of Coal Oil Point (Fig. 1). Terrain slopes gently towards the coast to the southwest and towards a lagoon to the  
420 south-southeast, rising again to the southeast of the COP bluffs. This flat relief likely has a small to negligible effect  
421 on wind speed and direction, although differential land-ocean heating could influence winds. Wind veering is likely  
422 for the coast to the east of COP due to the orientation of the coastline and bluffs.

423

Deleted: M

Deleted: m<sup>3</sup>

Deleted: Note

Deleted: to

Deleted: to

429 The WCS improvements in 2008 (Fig. 3 - dashed line) allowed for higher values of  $C$  and  $u$  (Supp. Fig. S7A, S7B).  
430 Comparison of the probability distributions of  $u$  and  $C$ ,  $\phi(u)$  and  $\phi(C)$ , respectively, before and after the upgrade  
431 suggested biases were not introduced (Supp. Fig. S7C, S7D). Specifically, changes in the average and median values  
432 and in the baseline after 2008 were from better measurement of higher value events (gusts and short positive  $C$   
433 anomalies).

Deleted: did not

434  
435 Significant daily, seasonal, and interannual variations are apparent in the day-averaged  $u$  and  $C$  (Fig. 3). The calmest  
436 season is late summer to fall, whereas spring is the windiest and most variable due to synoptic systems (Fig. 3A).  
437 Winds have strengthened since a minimum in 1995-1996, more so for the seep directions with stronger winds becoming  
438 more frequent and more so for summer than winter (Supp. Figs. S8, S9).

439  
440 Trends in  $C$  reflect trends in both seep field emissions and ambient  $C$ .  $C$  is higher in fall and spring (Fig. 3B). Given  
441 that stronger winds decrease  $C$  from seep emissions through dilution, this suggests the seasonal variation in  $C$   
442 underestimates the seasonal variation in emissions. Several studies have shown increased emissions under higher wave  
443 regimes (storminess), reviewed in Leifer (2019) and proposed to result from wave pumping. Storms increase evasion  
444 from higher wave turbulence and breaking-wave bubbles, which sparge dissolved  $\text{CH}_4$  and other trace gases as deep  
445 as the seabed in shallow (<100 m) waters (Shakhova, Semiletov, Salyuk, et al., 2010). Note,  $u$ ,  $\theta$ , and  $C'$  correlate  
446 with time of day. For example, north generally reflects weak (offshore) nocturnal winds with no seep contribution.  
447

Deleted: from

Deleted: be a

Deleted: of

Deleted: down

Deleted: to

Deleted: ,

### 448 3.2.2 Spatial heterogeneity

449 Calculating the angular-resolved average  $C$ ,  $C_{ave}(\theta)$ , for the complete dataset with respect to  $\theta$  shows the highest  $C$   
450 is from the main seep field direction (155-250°, Fig. 4). For the seep directions,  $C_{ave}(\theta)$  was poorly fit by a single  
451 Gaussian function but well fit ( $R^2 = 0.997$ ) by two Gaussian functions with peaks at 178° and 198° corresponding to  
452 the Seep Tent and Trilogy Seeps' directions, respectively (Figs. 4A, 4B). Notably, the fit residual showed a linear  
453 increasing trend,  $dC_{ave}(\theta)/d\theta$ , of 0.17 ppb degree<sup>-1</sup> from 180 to 210° (Supp. Fig. S9B) consistent with evasion from  
454 a dissolved downcurrent plume that drifts west-northwest along the coast (Leifer, 2019).

455  
456 The average  $C$  anomaly,  $C'_{ave}(\theta)$ , was calculated from the average of  $C_{Obs}(\theta)$ , after Eqn. 1, with terrestrial  
457 anthropogenic sources to from the north to northeast removed. The minimum in  $C_{Obs}(\theta)$  was at 270°, a direction with  
458 no mapped seepage that also is beyond the dissolved plume's approximate shoreward edge. Figs. 4A and 4B show  
459  $C_{Obs}(\theta)$  before removal of terrestrial emissions, which do not overlap in any significant manner with seep field  
460 emissions.

461  
462 There is a strong, focused peak in  $C_{max}(\theta)$  at  $\theta \sim 190^\circ$  (Figs. 4E, 4F), close to the Seep Tent Seep direction, 198°  
463 (Supp. Table S3), which is fairly isolated on the offshore seep trend (Fig. 1). This peak also is close to the direction  
464 of Tonya Seep on the inshore seep trend and close to the small, unnamed area of seepage to the west of Trilogy Seep

Deleted: (Figs. 4E, 4F)

473 on the Red Mountain Fault trend. The  $\theta$ -resolved maximum  $C(\theta)$ ,  $C_{max}(\theta)$ , remains elevated through  $\sim 270^\circ$ , far west  
474 of the  $C_{ave}(\theta)$  peak at  $\sim 200^\circ$ . This strongly suggests that the seep field extends further to the west-northwest than  
475 current maps [denote](#). These data cannot be explained by dissolved plume outgassing, which would affect  $C_{ave}(\theta)$  but  
476 not  $C_{max}(\theta)$ .

477  
478  $C(\theta)$  enhancements for non-seep directions (Fig. 4A, 4B) show a peak at  $\sim 35^\circ$ , corresponding to the direction of a  
479 commercial center amid suburban development. This could result from terrestrial seepage and natural gas pipeline  
480 leakage and/or *THC* emissions from communities and traffic.

481  
482 Neglecting the synoptic system, topographic forcing from the east-west Santa Ynez Mtn. range means that the  
483 strongest winds are the prevailing westerlies (Fig. 4C, 4D). North winds ( $320$ - $15^\circ$ ) largely are weak as are winds from  
484 due south; however, the sea breeze strengthens winds rapidly away from due south.  $\theta$  peaks in the maximum winds  
485 (1-minute sustained),  $u_{max}(\theta)$ , correspond to the west and east peaks in  $u_{ave}(\theta)$  with strengths to  $16 \text{ m s}^{-1}$ . Interestingly,  
486 there also are strong north ( $0$ - $30^\circ$ ) winds or downslope flow, termed sundowner winds, a highly localized and  
487 infrequent phenomenon. The overlap of  $u_{med}(\theta)$  and  $u_{ave}(\theta)$  shows winds largely are normally distributed.

488  
489 The median  $C$ ,  $C_{med}(\theta)$ , and average  $C$ ,  $C_{ave}(\theta)$ , have similar shapes, albeit with lower values at all  $\theta$  (Fig. 4A),  
490 indicating  $C$  is not normally distributed. This is shown in the wind direction-resolved wind speed probability  
491 distribution,  $\phi(\theta, u)$  (Fig. 5A), defined such that

492 
$$\int \phi(\theta, u) du = 1, \quad \int \phi(\theta, C) dC = 1. \quad (5)$$

493  $\phi(\theta, u)$  is very narrow ( $y$ -axis) for the northeast ( $\sim 45^\circ$ ) where winds are largely weak and broad for the east-southeast  
494 ( $70$ - $135^\circ$ ) and the prevailing westerlies ( $250$ - $280^\circ$ ). The east-southeast distribution skews to the south (stronger winds  
495 extend further from the south - offshore), whereas the prevailing westerly wind distribution skews to the northeast as  
496 does the coastline.

497  
498 In the seep direction,  $\phi(C, \theta)$  extends to much higher values than from non-seep directions (Fig. 5B).  $\phi(C, \theta)$  is  
499 asymmetric with  $\theta$  extending further to the west than the seep field extent ( $240^\circ$ ) and then decreasing more abruptly  
500 than the decrease to the east. This asymmetry is expected given the seep field's asymmetric orientation relative to  
501 WCS (eastern seepage is more distant). Emissions beyond the field's mapped western edge arise from downcurrent  
502 plume outgassing and potentially contributions from unmapped seeps.

### 504 3.2.3 Seep field diurnal emissions cycle

505  $C$  and  $u$  for the seep field direction,  $u_{seep}$ , and  $C_{seep}$ , respectively, follow diurnal patterns that are not the same as the  
506 overall diurnal pattern due to the wind direction constraint and because  $C_{seep}$  depends on  $u_{seep}$ . The dependency arises  
507 because higher  $u$  dilutes emissions, decreasing  $C$ , but higher  $u$  also increases dissolved plume evasion and bubble-

Deleted: (

Deleted: )

510 mediated emissions from higher swell (after a delay for wave build-up). Diurnal winds in coastal regions feature a  
511 shift between weak nocturnal offshore winds that veer to onshore winds in the morning - the sea breeze circulation.  
512 This was explored in time and direction segregated  $u$  and  $C$  ~~and explored for seep, direction-averaged  $u_{seep}$  and  $C_{seep}$~~   
513 for 90-270° (Fig. 6). Data were segregated by  $\theta$  for pre- and post-2008 (when station improvements facilitated better  
514 wind characterization, particularly for night winds, which are seldom from the seep field direction, see Supp. Fig. S10  
515 for 1991-2007).  $u(\theta, t)$  and  $C(\theta, t)$  were 2D Gaussian kernel smoothed with a 1-bin standard deviation (contours based  
516 on a 3-bin standard deviation) by the `imgaussfilt.m` algorithm (MATLAB, MathWorks, MA) after interpolating the  
517 calibration data gap 24:00-01:00.

518

519 Early morning (01:00-03:00)  $u_{seep}$  ~~is stronger because typical nocturnal winds are northerlies (land breeze), coming~~  
520 from the south largely during storms. These are accompanied by elevated  $C_{seep}$  implying greater emissions despite  
521 enhanced dilution from stronger winds. The minimum in both  $u_{seep}$  and  $C_{seep}$  occur in the early morning (04:00-08:00),  
522 with both increasing slightly through midday (~12:00).  $C_{seep}$  follows an afternoon trend of an overall decrease to a  
523 minimum at ~20:00 before increasing into the late evening.

524

525 Underlying these trends are complex temporal spatial patterns.  $C$  for the north to northeast reaches a maximum around  
526 noon ~~whereas  $u$  peaks around 16:00,  $C$  for the east is low in the morning, reaching a peak in the afternoon and likely~~  
527 reflects terrestrial sources. This pattern in  $C(t, \theta)$  extends to nearly 130°. Beyond the seep field's western edge,  $u$  is  
528 elevated from the prevailing direction (270°) with  $C$  elevated throughout the morning. There also is a short-lived peak  
529 in  $u$  around noon at ~300°, which corresponds to a short-lived depressed  $C$ . These could be consistent with wave  
530 development time, transport time, and sparging of the downcurrent plume; however, interpretation based on these  
531 patterns largely is speculative.

532

### 533 3.3 Overall seep field emissions

#### 534 3.3.1 Overall emissions

535 Average atmospheric emissions,  $E_A$ , for 1990-2020 were derived by an iterative Gaussian plume model, initialized  
536 with the 2005 sonar map (Fig. 7A). An emissions sensitivity study on the effect of grid resolution was conducted for  
537 resolutions from 11 to 225 m and a 22/56-m hybrid grid (Supp. Fig. S3). Simulations ~~turbulence parameters and~~  
538 stability class ~~were for moderate insolation~~ (Supp. Fig. S2), ~~and used~~ a 250-m  $BL$ , typical of Santa Barbara Channel  
539 marine values (Edinger, 1959; Rahn, Parish, & Leon, 2017). Simulation ~~angular resolution was 2°~~ (Hanna et al., 1982).  
540 Simulations were run iteratively until convergence, typically within 5 iterations (Supp. Fig. S11). Sensitivity studies  
541 found the distance weighting function,  $K(r, \theta)$ , was linear (Supp. Fig. S12).

542

543 Simulations could not reproduce observations in the Platform Holly direction ( $\theta=238^\circ$ ). Thus, a source was added for  
544 the platform area, which improved simulation-observational agreement in this wind direction. ~~Because significant~~

Deleted: and

Deleted: direction

Deleted: are

Deleted:  $u$

Deleted: and

Formatted: Font: Italic

Deleted: ; while

Deleted: northeast to

Deleted: to the east

Deleted: used moderate insolation to derive the turbulence

Deleted: and 2°

Deleted: Since

556 seep bubbles plumes generally are not observed in the platform's vicinity, these emissions could arise from incomplete  
557 combustion during flaring.

558

559 The model-derived,  $E_A$ , for 1990-2020 was 83,400  $\text{m}^3 \text{d}^{-1}$  (Fig. 7). Use of a composition-weighted *THC* molecular  
560 mass of 19.6  $\text{g mole}^{-1}$  implies 27 Gg *THC*  $\text{yr}^{-1}$ . Atmospheric seep gas is 88.5%  $\text{CH}_4$ , implying seep emissions of 19  
561 Gg  $\text{CH}_4 \text{ yr}^{-1}$  (Table 1). Given that  $\text{CH}_4$  is 73% of *THC*, non-methane hydrocarbon (NMHC:  $\text{C}_2\text{-C}_7$ ) emissions are 9,600  
562  $\text{m}^3 \text{d}^{-1}$  and gaseous emissions of 6.0 Gg  $\text{yr}^{-1}$ . For reference, Santa Barbara County 2018 Reactive Organic Carbon  
563 (ROC) emissions are listed at  $\sim 27$  tons  $\text{d}^{-1}$  (9.9 Gg  $\text{yr}^{-1}$ ) (ourair.org/emissions-inventory, SBAPCD). For our analysis,  
564 NMHC and ROC are the same. The largest NMHC was propane with emissions of 3510  $\text{m}^3 \text{d}^{-1}$ , followed by ethane at  
565 2590  $\text{m}^3 \text{d}^{-1}$ . The NMHC components of *THC* are conservative (do not react significantly) on the typical transport  
566 timescales from the seep field to WCS (20-30 minutes).

567

568 Seabed emissions,  $E_B$ , are necessarily significantly greater than  $E_A$  as  $E_A$  misses the fraction of emissions that remain  
569 in the water column,  $E_W$ , at least in the field's near downcurrent. There are two notes, the model  $E_A$  includes evasion  
570 from the dissolved plume in the area covered by the seep field sonar map. Secondly, the model does not include  $E_A$   
571 from the dissolved fraction that evades beyond the seep field extent. For the seep field area and near downcurrent area,  
572 Clark et al. (2000) estimated a 50:50 air/water partitioning based on a field study, implying  $E_B = 167,000 \text{ m}^3 \text{d}^{-1}$  for  
573 1990-2020 (54 Gg  $\text{yr}^{-1}$ ). A comparison of  $E_A$  versus  $\omega$  showed a very steep increase with  $\omega$  for  $E_A = 1\text{-}10 \text{ g s}^{-1} \text{ m}^2$  with  
574 rollover at  $\omega \sim 0.015$  (Supp. Fig. S13), which was approximately the noise level (Supp. Fig. S4).

575

576 Insights were provided by how the model partitioned emissions between different seep areas (Fig. 7). Particularly  
577 notable is the model's treatment of the Trilogy Seep area - the second strongest seep area after the Seep Tent Seep  
578 during the study period. The model re-assigned Trilogy Seep emissions to seepage to the west, representing Trilogy  
579 Seep emissions as unrealistically weaker than other, smaller seeps, such as IV Super Seep. One likely contributor to  
580 this re-assignment is wind veering (Supp. Fig. S14). Also suggesting wind veering is the model's assignment of strong  
581 emissions to the field's eastern and western edges despite weak sonar returns. In a comparison of the Seep Tent Seep  
582 and La Goleta Seep areas, the model emphasized the Seep Tent Seep whereas La Goleta Seep emissions were shifted  
583 to inshore seepage. This re-partitioning was greatly reduced for a  $+10^\circ$  wind veer, which also lessened the  
584 strengthening of emissions at the field's western edge relative to sonar. Given the lack of field data between the seep  
585 field and WCS on wind veering, further wind veering analysis was not conducted.

586

### 587 3.3.2 Seep field sector emissions

588 To investigate sub-field scale emissions, the seep field was segregated into three sectors: inshore, offshore east, and  
589 offshore west (Fig. 1). Based on integrating sonar return,  $\omega$ , inshore seepage contributes 40% of the field's  $\omega$  with the  
590 offshore seep trend split between 9% for the west and 51% for the east. Supporting this comparison is the similarity  
591 in the normalized sonar return probability distribution,  $\phi_s(\omega)$ , for the inshore seeps and offshore east seeps (Fig. 8). In

Deleted: ing

Deleted: seep emissions

Deleted: 022

Deleted: from

596 contrast,  $\phi_s(\omega)$  for offshore west seeps, differed dramatically despite the similarity in geology along the anticline  
597 underlying the offshore seep trend (Leifer et al., 2010). This likely results in part from the interaction between  
598 migration and production from Platform Holly. Although the normalized atmospheric emissions probability  
599 distribution,  $\phi_s(E_A)$ , for the inshore and offshore seeps are similar over most of the range (except the weakest,  $E_A < 0.02$   
600  $g\ s^{-1}$ ), significant differences are evident between offshore east and west seepage. Offshore east seepage is more  
601 dispersed and favors weaker seepage compared to offshore west seepage.

Deleted: age

603 The weakest seepage ( $\omega < 0.02$ ) contributed negligibly to overall sonar return and had no notable inshore-offshore  
604  $\phi_s(\omega)$  difference (Fig. 8). The largest difference is between the strongest seepage ( $\omega > 0.5$ ) for the inshore and offshore  
605 seeps. Specifically, there is a strong peak at  $\omega \sim 0.45$  and nothing stronger for the inshore seeps, whereas offshore  $\phi_s(\omega)$   
606 continued to  $\omega \sim 0.7$ . The  $E_A$  probability distribution,  $\phi_s(E_A)$ , for the strongest inshore seepage was similar to  $\phi_s(E_A)$  for  
607 strong offshore seepage. However, this masked a significant east-west offshore seepage difference. Specifically,  
608  $\phi_s(E_A)$  for strong seepage was reduced far more for the offshore east seeps than for the offshore west seeps, and the  
609 reverse for weak seeps.

Deleted: s

Deleted: seepage

Deleted: seepage

Deleted: seepage

611 The similarities of these distributions suggest that the controlling geological structures (fractures, fault damage zones,  
612 chimneys, etc.) are the same for inshore seepage and offshore east seepage, with the primary difference for the  
613 strongest seepage in these two sectors – the inshore Trilogy Seeps provide focused emissions, versus the offshore east  
614 La Goleta Seeps are comparatively dispersed and far oilier. Note, these seep areas are of similar strength.

Deleted: which are of similar strength

Deleted: whereas

616 Although,  $\omega$  is not  $E_A$ ,  $E_A$  followed the 40:60 partition in  $\omega$  between inshore and offshore seepage. Interestingly, the  
617  $E_A$  partitioning between the offshore east and offshore west differed significantly from sonar partitioning with 21% of  
618  $E_A$  from offshore west and 38% from offshore east. This greatly accentuated the  $E_A$  Seep Tent Seep area. In part, this  
619 arises from a diurnal cycle bias – WCS observes the offshore west seeps for afternoon/evening westerly winds, which  
620 are stronger, whereas WCS observes the offshore east seeps when winds are weaker, earlier in the day (Fig. 6B).  
621 Winds also increase bubble emissions from wave hydrostatic pumping and dissolved gas evasion. Also potentially  
622 contributing is saturation of  $\omega$  at very high bubble-density bubble plumes, primarily for the Seep Tent Seep and Trilogy  
623 Seep (Leifer et al., 2017). Saturation would imply an under-estimate of  $\omega$  for the strongest seep areas' emissions,  
624 which are for the west offshore seepage, altering the west: east  $\omega$  ratio (9%:51%).

Deleted: such as

### 626 3.3.3 Uncertainty and emissions sensitivity

627 Given the number of sources with poorly characterized variability, uncertainty is best assessed by Monte Carlo  
628 simulations; however, this was unfeasible due to the simulations' computational demands. Thus, emissions uncertainty  
629 was investigated by sensitivity studies (Fig. 9). Where data were available, uncertainty due to a specific parameter  
630 was estimated from the data. Specific parameters studied included sonar resolution, angular resolution,  $\delta\theta$ , wind speed,



639  $u$ , concentration anomaly,  $C'$ , boundary layer height,  $BL$ , wind veering,  $\psi$ , spatial northing offset,  $Y$ , and the inshore  
640 and offshore seepage partitioning,  $\zeta$ . Sensitivity study details are presented in Supp. Sec. S7.4.

641  
642 The contribution to uncertainty from  $\delta\theta$ ,  $C'$ ,  $\psi$ , and spatial offsets within the seep trends were minimal – just a few  
643 percent or less. Moderate uncertainty was identified for  $BL$  and  $\zeta$ . For example, for  $BL$  ranging from 150 to 350 m,  
644 mean  $E_A$  uncertainty was 6%. Although  $u$  has strong sensitivity, combined with  $BL$  its sensitivity is weak as  $u$  opposes  
645  $BL$  – lower  $u$  corresponds to higher  $BL$ . There still is uncertainty, though in the value of  $BL$ , which was not measured.  
646 Assessing uncertainty in  $\zeta$  was more challenging as there is no verification data on variability in the  $E_A$  partitioning  
647 between the inshore and offshore seep trends. The mean  $E_A$  uncertainty for  $-50% < \zeta < 50%$  is 11.5% from a polynomial  
648 fit. Still, the consistency in seepage location between sonar surveys spanning decades (Leifer, 2019) suggests only  
649 modest changes in  $\zeta$  over the multi-decade time period of model averaging. Total uncertainty was taken as 15% based  
650 on the sum of uncertainty in  $BL$  and  $\zeta$ , each averaged to the nearest 5%.

### 652 3.4 Ellwood Field emissions

653  $C(\theta)$  increases to the northeast with a peak at 290-320° corresponding to the direction towards abandoned wells off  
654 Haskell Beach (Fig. 10). Emissions from this area – either from natural seepage or leaking wells – were noted in the  
655 offshore survey data near Haskell Beach (Fig. 2A). Additionally,  $C_{max}(\theta)$  shows a 22-ppm peak in this direction  
656 well above  $C_{ave}(\theta)$  (Fig. 4F). This is consistent with transient releases from natural seep and/or abandoned well  
657 emissions.

658  
659 Ellwood field production continued through the 1970s with wells drilled into the geological structures that allowed  
660 oil accumulation (Olson, 1983), including faults that provide migration pathways (Leifer et al., 2010). There are many  
661 abandoned wells from these oil fields and others on the Goleta Plains, beaches, and shallow near-coastal waters to the  
662 west-northwest of WCS (offshore Haskell Beach and onshore around Naples Point). Currently, active wells only are  
663 found at the La Goleta Gas field (a natural gas storage field), east of WCS.

664  
665 Faults associated with these anticlines provide migration pathways and are aligned approximately with the coast in a  
666 series of roughly parallel faults extending onshore (Minor et al., 2009). The onshore/coastal Ellwood field (northwest  
667 of the South Ellwood field) sources from the primarily sandstone Vaqueros Formation (Olson, 1983), whose main  
668 trap is an anticline at the western edge of the North Branch Western More Ranch Fault (NBWMRF). Offshore seepage  
669 tracks some of these faults, e.g., the Isla Vista Fault trend corresponds to an offshore seep trend in Goleta Bay that  
670 includes the Goleta Pier Seep, whereas wells follow the NBWMRF trend offshore of Haskell Beach.

671

Deleted: does not

Deleted: counters

Deleted: is

Deleted: ),

Deleted: from others fields

Deleted: approximately

678 4 Discussion

679 4.1 Atmospheric seep field observations

680 4.1.1. Air quality station

681 A range of approaches are available to evaluate marine seepage CH<sub>4</sub> emissions. Specifically, *in situ* approaches  
682 including direct capture (Leifer, 2015; Washburn, Johnson, Gotschalk, & Eglund, 2001), fluid flow measurements  
683 (Leifer & Boles, 2005), video (Leifer, 2015), and remote sensing approaches that include active acoustics, i.e., sonar  
684 (Homafius et al., 1999), dissolved *in situ* (Marinero et al., 2006), and passive acoustics (Wiggins et al., 2015). Remote  
685 sensing is the best approach for long-term monitoring to capture shifts in emissions between vents. To date, only sonar  
686 remote sensing has provided quantitative seep plume (seabed) emissions (Homafius et al., 1999). Notably, sonar  
687 ranges are up to a few hundred meters, far less than the size scales of many seep fields, whereas high power demands  
688 typically require a cabled observatory for long-term observations.

Deleted: :

689  
690 This study demonstrated that air quality station data can provide the long-term continuous data needed to capture  
691 seasonal variations including emissions during storms and transient events, which field campaigns likely miss. For  
692 example, sonar surveys generally are scheduled during summer when seas are calmer and winds more predictable and  
693 when seepage is weakest (Fig. 3); however, not during storms when emissions likely are enhanced.

694  
695 The approach presented in this study derived atmospheric trace gas emissions from long-term air quality and  
696 meteorology data for a dispersed area source that is constrained by sonar seepage maps. This approach can be extended  
697 to terrestrial seepage if the source can be constrained spatially (e.g., by geology); although nearby anthropogenic  
698 sources may complicate emissions assessments. Other terrestrial sources such as landfills, O&G production fields, or  
699 industrial sites – if spatially constrained – could be addressed by this approach, particularly if isolated from other  
700 confounding sources. The use of cavity enhanced absorption spectrometers that can speciate gases like CH<sub>4</sub> and C<sub>2</sub>H<sub>6</sub>  
701 could enable discrimination some confounding sources as well as better characterization of emissions. Although  
702 onshore stations can address nearshore seepage, further offshore seepage could be addressed by a moored station.  
703 Moored stations also could include *in situ* aqueous chemical sensors and current measurements.

Deleted: from long-term air quality and meteorology data

Deleted: due to

Deleted: that

Deleted: an

Deleted: ,

705 4.1.2 *In situ* atmospheric surface surveys

706 Atmospheric emissions were assessed for three seep areas ~~at~~ a zone of focused seepage - by an atmospheric *in situ*  
707 survey approach wherein downwind data are collected orthogonal to the wind direction in a transect that spans the  
708 plume (background to background on the plume's edges). This approach was developed for terrestrial sources (Leifer,  
709 Melton, Tratt, et al., 2018) yet remains unused for offshore marine seepage, which often are area sources. In this study,  
710 this was addressed by gridding the area source and treating each grid as a far-field point source. Gaussian plume  
711 inversion requires distant point source(s), i.e., far field. Downwind *in situ* transects of three strong seep areas all were  
712 well characterized by the Gaussian plume model.

Deleted: -

720

721 One advantage of atmospheric surveys is rapidity - a single transect of a few minutes is sufficient to derive emissions  
722 for a seep area. In comparison, a flux buoy survey can require many hours to a day (Clark et al., 2010), during which  
723 forcing factors (waves, tides, etc.) change significantly. Seep area sonar surveys also are rapid (Wilson, Leifer, &  
724 Maillard, 2015) allowing a combined sonar and atmospheric survey to repeat characterize emissions and sea-air  
725 partitioning within a few hours. With respect to the entire COP seep field, whereas a sonar survey requires two to  
726 three days (Leifer et al., 2010), a downwind atmospheric survey is far more rapid, requiring perhaps an hour. This  
727 allows repeat field emissions measurements over a tidal cycle.

728

## 729 4.2 Seep field emissions

### 730 4.2.1 Total emissions

731 To date, only two estimates of COP seep field seabed emissions,  $E_B$ , have been published. Hornafius et al. (1999)  
732 estimated  $E_B=1.5 \times 10^5 \text{ m}^3 \text{ dy}^{-1}$  (64 Gg  $\text{yr}^{-1}$ ) based on sonar surveys covering 18 km<sup>2</sup> from Nov. 1994 – Sep. 1996,  
733 collected during the summer to late fall seasons. This value excluded Seep Tent collection. A 4.1 km<sup>2</sup> sonar survey in  
734 Aug.-Sep. 2016 estimated  $E_B=24,000 \text{ m}^3 \text{ dy}^{-1}$  (Padilla, Loranger, Kinnaman, Valentine, & Weber, 2019), significantly  
735 lower. In part, this arises from field subsampling, but also could arise from long-term changes. Notably, neither study  
736 addressed temporal variability. The sonar surveys occurred in summer and fall when seepage activity is at a minimum,  
737 whereas winter and early spring feature much higher activity associated with storms (Bradley et al., 2010).

738

739 Hornafius et al. (1999) used an engineered bubble plume to calibrate emissions, an approach also used in Leifer et al.  
740 (2017). Due to technology limitations at the time, the strongest seepage was clipped / saturated, i.e., underestimated,  
741 and the survey did not cover shallow seepage. Thus, the Hornafius et al. (1999) emissions estimate is a lower limit for  
742 summer/fall emissions. The Padilla et al. (2019) survey was calibrated by an inverted seep flux buoy suspended at 23  
743 m. This differs significantly from the seep flux buoy measurement approach reported in Washburn et al. (2001), which  
744 were collected in surface drift mode. Surface drift mode ensures a horizontal orientation for the buoy and an absence  
745 of lateral velocity difference between the capture device and currents – either of which decreases capture efficiency  
746 from 100%, biasing derived emissions low. Further, the Padilla et al. (2019) survey was calibrated 1 month after the  
747 sonar surveys, whereas the 1995 engineered plume calibration by Hornafius et al. (1999) was contemporaneous. The  
748 Hornafius et al. (1999) approach accounts, in part, for dissolution between the seabed and survey depth window - it  
749 uses air rather than CH<sub>4</sub>, which dissolves slower than CH<sub>4</sub>. Dissolution losses for CH<sub>4</sub> between the seabed and the  
750 depth window can be addressed by a numerical bubble model (Leifer et al., 2017).

751

752 The Gaussian plume model-derived  $E_A$  was  $8.3 \times 10^4 \text{ m}^3 \text{ dy}^{-1}$ . Based on the Clark et al. (2000) assessment that half the  
753 seabed seepage reaches the atmosphere,  $E_B=1.7 \times 10^5 \text{ m}^3 \text{ dy}^{-1}$ ; very similar to  $E_B=1.5 \times 10^5 \text{ m}^3 \text{ dy}^{-1}$  from Hornafius et al.  
754 (1999). This agreement is coincidental as it neglects seasonal and interannual trends. For example, Bradley et al.  
755 (2010) found 1994-1996 emissions were well below the average for 1990-2008, increasing significantly after 2008.

Deleted: Also rapid are s

Deleted: ,

Deleted: which i

Deleted: ;

Deleted: however

Deleted: large transient events and

Deleted: or

Deleted: are

Deleted: d

Deleted:

766

#### 767 4.2.2 Methane and non-methane hydrocarbon emissions

768 Analysis of atmospheric samples provided a picture of the complexity of atmospheric emissions that arises from the  
769 multiple pathways underlying atmospheric emissions. Specifically, as bubbles rise, they lose lighter and more soluble  
770 gases faster (deeper in the water column), leading to differences between evasion from dissolved gases and direct  
771 bubble transport (Leifer & Clark, 2002). Thus, bubble-mediated transport enhances larger alkanes relative to smaller  
772 alkanes leaving more of the smaller alkanes in the water column. For strong seeps, bubble plumes are associated with  
773 strong upwelling flows (Leifer et al., 2009), which transport dissolved gases to the sea surface where they outgas.  
774 Additionally, oil (as droplets and bubble coatings) enhances alkane transport due to slower dissolution and diffusion  
775 of larger alkanes through oil.

776

777 Atmospheric plume concentrations were 11.5% *NMHC* and 88.5%  $\text{CH}_4$ , very similar to Hornafius et al. (1999) who  
778 referenced the Seep Tent composition (88%  $\text{CH}_4$ , 10% *NMHC*, and 2% nitrogen) as very similar to the reservoir  
779 composition. Note, Clark et al. (2010) observed near sea surface bubbles from Trilogly with 5.7% to 7.9% *NMHC* and  
780 52.4 to 79.7%  $\text{CH}_4$ , demonstrating significant partitioning. The similarity between the atmospheric and seabed  
781 composition demonstrates efficient dissolved gas transfer to the sea surface despite the difference in the bubble  
782 composition.

783

784 COP seep field seabed emissions are orders of magnitude greater than typically reported for other seep areas, e.g., the  
785 summary in Römer et al. (2017) where emissions for 12 different seep areas including sites in the North Sea, Pacific  
786 northwest, Gulf of Mexico, and other areas were 2-480 tons  $\text{yr}^{-1}$ , multiple orders of magnitude less than COP seep  
787 field seabed emissions. Römer et al. (2017) used a bubble model for Dogger Bank seepage in the North Sea to estimate  
788 emissions for observed atmospheric  $\text{CH}_4$  plumes. The model estimated direct atmospheric bubble-mediated emissions  
789 of 21.7 ton  $\text{yr}^{-1}$ , 20% of seabed emissions. For the Tommelieten Seeps (in 70-m water) Schneider von Deimling et al.  
790 (2011) estimated 4% of the 0.024 Gg  $\text{CH}_4 \text{ yr}^{-1}$  seabed emissions, i.e.,  $\sim 1 \text{ Mg } \text{CH}_4 \text{ yr}^{-1}$  reached the atmosphere by  
791 bubble-mediated transfer. Schneider von Deimling et al. (2011) used a bubble model based on an assumed bubble size  
792 and neglected diffusive flux. These diffusive fluxes include bubble dissolution into the wave-mixed layer in the local  
793 area. A few studies have directly measured atmospheric fluxes by an air-sea gas transfer model. For example, Schmale,  
794 Beaubien, Rehder, Greinert, and Lombardi (2010) found seep air fluxes of 0.96-2.32  $\text{nmol m}^{-2} \text{ s}^{-1}$ , much higher than  
795 the ambient Black Sea flux of 0.32-0.77  $\text{nmol m}^{-2} \text{ s}^{-1}$ . In the Black Sea, ambient emissions arise from microbially  
796 produced  $\text{CH}_4$  in shelf and slope sediments (Reeburgh et al., 1991). Di, Feng, and Chen (2019) estimated 7.7  $\text{nmol m}^{-2} \text{ s}^{-1}$   
797 for the shallow South China Sea based on an air-sea gas transfer model. If we disperse COP seep field atmospheric  
798 emissions of  $1.15 \times 10^9 \text{ M yr}^{-1}$  over the  $\sim 6.3 \text{ km}^2$  of  $25 \times 25 \text{ m}^2$  bins with emissions, we find  $5.7 \text{ } \mu\text{M m}^{-2} \text{ s}^{-1}$ , three orders  
799 of magnitude greater.

800

Deleted: Trilogly

Deleted: despite the difference in the bubble composition

Deleted: etc.,

Deleted: wave

805 Recent estimates of total global geo-CH<sub>4</sub> sources from a bottom-up approach are 45 Tg yr<sup>-1</sup> with submarine seepage  
806 contributing 7 Tg yr<sup>-1</sup> (Etiopie & Schwietzke, 2019), implying [that the](#) COP seep field contributes ~0.27% of global  
807 submarine emissions. However, an estimate of pre-industrial CH<sub>4</sub> emissions (not confounded with fossil fuel  
808 production emissions) based on ice core <sup>14</sup>CH<sub>4</sub> suggested 1.6 Tg geo-CH<sub>4</sub> yr<sup>-1</sup> emissions (Hmiel et al., 2020). This  
809 estimate, if accurate, would imply the COP seep field contributes an astounding 1% of global seep emissions  
810 (submarine and aerial) and is difficult to reconcile with the COP seep field and [seepage estimates for other high](#)  
811 [emission seep fields](#). For example, CH<sub>4</sub> atmospheric emissions for the Lusi hydrothermal system [was estimated at](#) 0.1  
812 Tg yr<sup>-1</sup> (Mazzini et al., 2021), a hotspot in the Laptev Sea, [was estimated at](#) 0.9 Tg yr<sup>-1</sup> into shallow seas (Shakhova,  
813 Semiletov, Leifer, et al., 2010), and [emissions for](#) the East Siberian Arctic Sea using eddy covariance of 3.0 Tg yr<sup>-1</sup>  
814 (Thornton et al., 2020).

815  
816 COP seep field C<sub>2</sub>H<sub>6</sub> emissions were 1.27 Gg C<sub>2</sub>H<sub>6</sub> yr<sup>-1</sup>. For reference, this is 11% of the 11.4 Gg C<sub>2</sub>H<sub>6</sub> yr<sup>-1</sup> in 2010  
817 for the South Coast Air Basin (SCAB), which includes Los Angeles (Peischl et al., 2013). Globally, Simpson et al.  
818 (2012) and Höglund-Isaksson (2017) found 11.3 and 9.7 Tg C<sub>2</sub>H<sub>6</sub> yr<sup>-1</sup> in 2010, respectively. C<sub>2</sub>H<sub>6</sub> has been increasing  
819 since 2010 due to increased O&G production emissions (Helmig et al., 2016). Globally, seeps are estimated to  
820 contribute 2-4 Tg C<sub>2</sub>H<sub>6</sub> yr<sup>-1</sup> (Etiopie & Cicciooli, 2009), and from ice cores, 2.2-3.5 Tg yr<sup>-1</sup> (Nicewonger, Verhulst,  
821 Aydin, & Saltzman, 2016). This suggests the COP seep field contributes 0.03-0.06% of global seep [C<sub>2</sub>H<sub>6</sub>](#) emissions.  
822

823 Seep THC was 4.2% [C<sub>3</sub>H<sub>8</sub>](#), implying emissions of 2.5 Gg C<sub>3</sub>H<sub>8</sub> yr<sup>-1</sup>. Global propane emissions are 10.5 Tg yr<sup>-1</sup> (Pozzer  
824 et al., 2010), with 1-2 Tg yr<sup>-1</sup> estimated for seeps (Etiopie & Cicciooli, 2009). This suggests the COP seep field  
825 contributes 0.05-0.1% of the global seep budget. Oceans are estimated to contribute 0.35 Tg C<sub>3</sub>H<sub>8</sub> yr<sup>-1</sup> (Pozzer et al.,  
826 2010), less than geological seepage contribution.  
827

828 Based on an evaluation of the COP seep field emissions with respect to global seep ethane and propane emissions, [the](#)  
829 COP seep field contribution to global geo-CH<sub>4</sub> emissions are consistent with recent global geo-gas CH<sub>4</sub> emissions  
830 estimates of 45 Tg yr<sup>-1</sup> (0.04%) (Etiopie et al., 2019) [and](#) not the significantly lower pre-industrial estimates of global  
831 geo-CH<sub>4</sub> emissions, e.g., 1.6 Tg yr<sup>-1</sup> (1.15%) (Hmiel et al., 2020).  
832

833 Global butane emissions are 14 Tg C<sub>4</sub>H<sub>10</sub> yr<sup>-1</sup> (Pozzer et al., 2010), higher than ethane and propane. COP seep field  
834 butane (C<sub>4</sub>) and pentane (C<sub>5</sub>) emissions were 2.2 Gg C<sub>4</sub>H<sub>10</sub> yr<sup>-1</sup> and 1.1 Gg C<sub>5</sub>H<sub>12</sub> yr<sup>-1</sup>, respectively, with combined  
835 C<sub>2</sub>-C<sub>5</sub> emissions of 7.1 Gg yr<sup>-1</sup>, compared to 65 Gg yr<sup>-1</sup> from the entire SCAB, i.e., COP seep field contributes ~5%  
836 the SCAB. COP C<sub>2</sub>-C<sub>5</sub> emissions are significantly above that of the La Brea area, estimated at 1.7 Gg yr<sup>-1</sup> (D. Weber  
837 et al., 2017). Note, COP seep field atmospheric C<sub>2</sub>-C<sub>5</sub> emissions certainly are larger, potentially significantly, as larger  
838 alkanes also are emitted from oil slicks but were not considered for this study, and furthermore, the atmospheric plume  
839 from the slicks was not sampled for this study.  
840

Deleted: other top

Deleted: of

Deleted: of

Deleted: for

Deleted: of

Deleted: Thus, COP seep field emissions either play a significant role in global seep emissions or indicate that geo-gas emissions are less tightly constrained than Hmiel et al. (2020).

Deleted: propane

Deleted: ,

Deleted: ,

852 Both benzene and toluene were detected with estimated emissions of 8300 and 2300 kg yr<sup>-1</sup>, respectively. These  
853 emissions likely are underestimates, potentially significantly, due to neglecting the oil slick evaporation contribution.  
854 Both gases are of significant health concerns, as are alkanes like pentane and hexane.  
855

#### 856 4.3 Downcurrent emissions

857 The seep field concentration,  $C(\theta)$ , anomaly was centered at  $\theta=200^\circ$  ~~the Seep Tent Seep (198° - Supp. Table S3)~~,  
858 and was well described by a dual Gaussian function (Fig. 4B). This was surprising given that the seep field is  
859 asymmetric with respect to a 200° axial line from WCS to COP. Underlying this seeming discrepancy is that WCS  
860 winds are weakest from due south and strongest from the west (prevailing) and also stronger to the east-southeast (Fig.  
861 4C).  
862

863 The residual of the Gaussian fit increased in the downcurrent direction (Supp. Fig. S9B), consistent with evasion from  
864 the downcurrent dissolved plume and seepage from this area. The dissolved plume roughly follows the coast,  
865 extending as far as ~280° from WCS due to the coastline shift from northwest to west around Haskell Beach (Fig. 10),  
866 ~30° beyond the seep field's sonar mapped western edge (Fig. 1). As prevailing winds are westerlies (paralleling the  
867 coastal mountains), downcurrent plume evasions decrease with distance due to dispersion and as surface waters  
868 become depleted by evasion. Evasion increases non-linearly with  $u$ , particularly for winds that include wave breaking  
869 (Nightingale et al., 2000); however, higher winds also dilute emissions. Note, there are no mapped seeps in this area.  
870

871 Dissolved plume emissions also likely occur from east of the field, leading the model to emphasize seepage at the  
872 field's eastern extent, too. Specifically, strong prevailing afternoon westerly surface winds drive a near-surface  
873 dissolved plume eastwards. When these westerly winds calm down late in the evening, easterly winds transport  
874 evasion from this east-displaced dissolved plume towards WCS. Additionally, it also is possible that the COP seep  
875 field extends further east than mapped in sonar surveys, at least during some seasons.  
876

#### 877 4.4 Focused seep area emissions

878 Trilogy Seep area emissions were estimated at 6,200 m<sup>3</sup> CH<sub>4</sub> dy<sup>-1</sup> in May 2016. For comparison, Clark et al. (2010)  
879 found 5500 and 4200 m<sup>3</sup> THC dy<sup>-1</sup> (4,900 and 3,700 m<sup>3</sup> CH<sub>4</sub> dy<sup>-1</sup>) for Trilogy Seep as measured by a flux buoy for  
880 near surface bubble fluxes in Sept. 2005. Note, the plume inversion approach also includes outgassing of near surface  
881 waters that have enhanced  $C_{CH_4}$  from plume dissolution, which the flux buoy approach does not include. Although  
882 Clark et al. (2010) found surface bubbles had undetectable CO<sub>2</sub>, the atmospheric plume's CO<sub>2</sub> to CH<sub>4</sub> concentration  
883 ratio was comparable to the seabed bubble concentration ratio. This demonstrates ~~efficient~~ upwelling flow transport  
884 of seabed water to the sea surface where dissolved gases evade near where the bubble plume surfaces. This near-plume  
885 evasion contributes to the atmospheric plume. Note, these emissions neglect downcurrent emissions. A 50:50

Deleted: .

Deleted: and well

Deleted: matched

Deleted: location of

Deleted: the seep field well

Deleted: moreover,

Deleted: also

Deleted: significant

894 atmosphere:ocean partitioning suggests 2016 Trilogy Seep emissions were ~40% lower than in 2005 – a difference  
895 within the difference between the two 2005 Trilogy Seep measurements by Clark et al. (2010).

896

897 In contrast, agreement was very poor for the Seep Tent Seep, for which Clark et al. (2010) mapped emissions of 5700  
898 m<sup>3</sup> day<sup>-1</sup> (5000 m<sup>3</sup> CH<sub>4</sub> day<sup>-1</sup>) in Nov. 2002 whereas this study found 310 m<sup>3</sup> CH<sub>4</sub> dy<sup>-1</sup>. This discrepancy was readily  
899 apparent with almost no visible surface bubble expression in May 2016, whereas the Seep Tent Seep has been a  
900 perennial feature since its appearance. The absence of more than a few scattered bubbles at the sea surface (the boil  
901 in 2000 was driven by a 1-2 m s<sup>-1</sup> upwelling (Leifer, Clark, & Chen, 2000), which, indicates that most emissions are  
902 from evasion. A buoyancy plume associated with the rising oil droplets (thick oil slicks surface above the Seep Tents)  
903 as well as CH<sub>4</sub> dissolved in the oil likely are transporting the observed, focused CH<sub>4</sub> emissions.

904

905 This is remarkable given that the seep field’s geofluid migration “center” in recent decades has been the Seep Tent  
906 Seep (Bradley et al., 2010), which was the largest seep in the field in 2010 (Clark et al., 2010). The Seep Tent Seep  
907 consists of emissions not captured by the Seep Tents – two large (33-m square) steel capture tents on the seafloor. For  
908 reference, the Seep Tents captured ~16,800 m<sup>3</sup> gas dy<sup>-1</sup> in the early 2000s (Boles et al., 2001). Bradley et al. (2010)  
909 found in WCS data that when overall seep field emissions decreased to a minimum in 1995, they were focused on the  
910 Seep Tent Seep direction. Note, the Seep Tent Seep was observed first in 1970 as a boil visible from 1.6-km distant.  
911 The Seep Tent Seep was tented in Sept. 1982 (Boles et al., 2001).

912

913 Underlying these observations are several factors. First, the Seep Tent Seep is modern – since 1978 – as it was not  
914 mapped in a 1953 seep survey (Leifer, 2019). At the time, it was first reported as a sea boil visible over a kilometer  
915 distant (Boles et al., 2001). Since installation, overall Seep Tent production has diminished (Boles et al., 2001) by a  
916 factor of 3 from 1984 to 1995. Some fraction of this trend could have resulted from the expansion of active seepage  
917 beyond the seep tents. Perhaps more significantly, the Seep Tent Seep lies over one of the Platform Holly wells (Leifer  
918 et al., 2010; Fig. 3C), creating the potential of linkage between well production (including stimulation) and Seep Tent  
919 production and thus Seep Tent seepage (the uncaptured portion).

920

#### 921 4.6 Diurnal trend and bias

922 The diurnal wind patterns typical of the coastal Pacific marine environment are weak offshore (northerly) night winds  
923 that shift to from the east in the morning and then further shift to from the south. In afternoon they strengthen and shift  
924 to prevailing westerlies, continuing to late in the evening (Bradley et al., 2010). Note, WCS seep emissions require  
925 winds to “probe or scan” across the seep field, and thus miss the strong afternoon prevailing winds when emissions  
926 are expected to be higher. This is because higher wind speeds increase sea-air gas emissions of dissolved near-surface  
927 gases (Nightingale et al., 2000) and increase emissions from higher hydrostatic pressure fluctuation driven by wave  
928 height (Leifer & Boles, 2005). Given that prevailing winds are westerlies, higher afternoon emissions will generally  
929 (but not always) drift eastwards, missing WCS.

Deleted: - (Leifer, Clark, & Chen, 2000)

Deleted: -

Deleted: seep

Deleted: swing

934

935 The diurnal wind pattern from the seep field direction is different from the overall (direction-independent) diurnal  
936 pattern. Typical nocturnal winds are quite weak, 1.5–1.7 m s<sup>-1</sup> (Fig. 6). The strongest diurnal wind change was from  
937 late night to morning, a 20% decrease. Onshore winds (seep direction) in the middle of the night are from synoptic  
938 systems and were associated with the highest *C*. Winds increase by a few percent to an early afternoon peak,  
939 decreasing through early evening before increasing again later in the night.

940

941 The diurnal trend for *C* from the seep direction followed the diurnal wind cycle, increasing by ~20 ppb and peaking  
942 ~2 hours later in the day than winds (15:00 versus 13:00 for *C* compared to *u*, respectively). This may reflect the lag  
943 in wave development with respect to wind strengthening and transport time. Based on sensitivity studies, the diurnal  
944 cycles in *u* and *C* correspond to variations of ~7% and ~9% in *E<sub>A</sub>*.

945

946 Although efforts were made to characterize the diurnal cycle from WCS data, WCS data poorly sample the seep field  
947 for the higher wind speeds that occur in the afternoon which primarily are westerlies. Note, non-linearity in sea-air  
948 evasion with *u* means the model use of average *u* underestimates *E<sub>A</sub>*. Thus, the contribution of the prevailing afternoon  
949 winds to diurnal emissions is significantly underestimated from WCS data. It is worth noting, though, that this factor  
950 only affects 25–33% of diurnal emissions. As the true diurnal cycle cannot be derived from WCS data, repeat field  
951 transects spanning the different phases of a diurnal cycle are needed.

952

#### 953 4.7 Future needs and improvements

954 The sensitivity studies identified areas for improvement and data gaps. These are described in brief below and in more  
955 detail in Supp. Sec. S8. The largest uncertainty was with regards to partitioning between the inshore and offshore seep  
956 trends, which could be determined by a second air quality station, preferably including speciation such as by CEAS  
957 analyzers of CH<sub>4</sub>, C<sub>2</sub>H<sub>6</sub>, and C<sub>3</sub>H<sub>8</sub>. Further simulations could add grid cells for evasion corresponding to the  
958 downcurrent plumes to assess their contribution. The model was limited by available workstation power; however,  
959 additional computation power could open improvements such as simulating a range of wind speeds based on the wind  
960 speed probability distribution with respect to wind direction,  $\phi(u, \theta)$ , e.g., Fig. 5.

961

962 Additional field work and data also are needed. Another important sensitivity was to boundary layer height, *BL*, which  
963 varies diurnally and seasonally (Dorman & Winant, 2000) and could be derived from ceilometer data (Münkel, 2007).  
964 Another significant concern is afternoon seep field emissions that bypass WCS, which could be addressed by field  
965 work and a second air quality station at a different downwind direction from the seep field. Mapping offshore wind  
966 fields to characterize wind veering across the seep field is needed to allow simulations to provide insights at the seep  
967 area size-scale.

968

Deleted: field data of



970 **5 Conclusions**

971 In this study, data from an onshore air quality station located downwind of a large marine seep field was analysed to  
972 derive the three-decade-averaged seep field emissions using an inversion model. The modeled emissions were similar  
973 to reported emissions; however, this was coincidental given that prior reported emissions were during a period of field  
974 quiescence. Highlighting the significance of the COP seep field, ethane and propane emissions suggest the COP seep  
975 field contributes 0.04% and 0.12% of the global seep budget, respectively. As a result, COP seep field emissions of  
976 19 Gg CH<sub>4</sub> yr<sup>-1</sup> are consistent with global geo-gas budgets of 45 Tg yr<sup>-1</sup>, but inconsistent with significantly lower  
977 emissions estimated from ice core isotopic data. Additionally, the approach could be adapted to air quality station data  
978 for other sources including terrestrial seeps, production fields, etc., if the sources are spatially constrained and isolated  
979 from confounding sources.

980

981 **Data availability.** All data needed to evaluate the conclusions in the paper are present in the paper and/or the  
982 Supplementary Materials and/or were submitted to the Mendeley Data Repository, see Leifer, Ira (2020),  
983 "Seep\_Air\_Data", Mendeley Data, V1, <http://dx.doi.org/10.17632/znhxkftm8.1>

984

985 **Supplement.** The supplement contains additional supporting figures and details to complement the manuscript and  
986 an interactive map file as a Google Earth archive of the offshore survey data that are presented in **Fig. 2**.

987

988 **Author Contributions.** IL Developed and conducted the study, analysed data, and wrote the manuscript. CM analysed  
989 data and edited the manuscript. DB analysed air sample data and edited the manuscript.

990

991 **Competing interests.** The authors declare that they have no conflict of interest.

992

993 **Acknowledgements.** We would like to gratefully acknowledge the SBCAPCD for providing data from their ongoing  
994 monitoring program and the contribution of Marc Moritsch and Joel S. Cordes in particular for help with these data,  
995 and Doug Wilson for the processed sonar data. We recognize the skill and participation of vessel captains Jeff Wright  
996 and Tony Vultaggio and editorial review by Charlotte Marston, Bubbleology Research International.

997

998 **Financial Support.** This work was supported by Plains All American Pipeline and the Bubbleology Research  
999 International, Internal Research and Development (IRAD) fund.

1000

1001 **References**

- 1002 Abrams, M. A. (2005). Significance of hydrocarbon seepage relative to petroleum generation and  
1003 entrapment. *Marine and Petroleum Geology*, 22(4), 457-477.  
1004 doi:10.1016/j.marpetgeo.2004.08.003
- 1005 Abrams, M. A. (2017). Evaluation of near-surface gases in marine sediments to assess  
1006 subsurface petroleum gas generation and entrapment. *Geosciences*, 7(2), 35.  
1007 doi:10.3390/geosciences7020035
- 1008 Bernard, B. B., Brooks, J. M., & Zumberge, J. (2001, 16-19 September 2001). *Determining the*  
1009 *origin of gases in near-surface sediments*. Paper presented at the AAPG Hedberg  
1010 Conference, Vancouver BC, Canada.
- 1011 Boles, J. R., Clark, J. F., Leifer, I., & Washburn, L. (2001). Temporal variation in natural  
1012 methane seep rate due to tides, Coal Oil Point area, California. *Journal Geophysical*  
1013 *Research - Oceans*, 106(C11), 27,077-027,086. doi:10.1029/2000JC000774
- 1014 Borges, A. V., Champenois, W., Gypens, N., Delille, B., & Harlay, J. (2016). Massive marine  
1015 methane emissions from near-shore shallow coastal areas. *Scientific Reports*, 6, 27908.  
1016 doi:10.1038/srep27908
- 1017 Bradley, E. S., Leifer, I., & Roberts, D. A. (2010). Long-term monitoring of a marine geologic  
1018 hydrocarbon source by a coastal air pollution station in Southern California. *Atmospheric*  
1019 *Environment*, 44(38), 4973-4981. doi:10.1016/j.atmosenv.2010.08.010
- 1020 CDOGGR. (2018). Well Finder. Retrieved from  
1021 <https://www.conservation.ca.gov/dog/Pages/Wellfinder.aspx>. Retrieved 6 May 2019,  
1022 from California Department of Conservation  
1023 <https://www.conservation.ca.gov/dog/Pages/Wellfinder.aspx>
- 1024 Ciotoli, G., Procesi, M., Etiopie, G., Fracassi, U., & Ventura, G. (2020). Influence of tectonics on  
1025 global scale distribution of geological methane emissions. *Nature Communications*,  
1026 11(1), 2305. doi:10.1038/s41467-020-16229-1
- 1027 Clark, J. F., Washburn, L., Hornafius, J. S., & Luyendyk, B. P. (2000). Natural marine  
1028 hydrocarbon seep source of dissolved methane to California coastal waters. *Journal*  
1029 *Geophysical Research - Oceans*, 105, 11,509-511,522. doi:10.1029/2000JC000259
- 1030 Clark, J. F., Washburn, L., & Schwager, K. (2010). Variability of gas composition and flux  
1031 intensity in natural marine hydrocarbon seeps. *Geo-Marine Letters*, 30, 379-388.  
1032 doi:10.1007/s00367-009-0167-1
- 1033 Di, P., Feng, D., & Chen, D. (2019). The distribution of dissolved methane and its air-sea flux in  
1034 the plume of a seep field, Lingtuo Promontory, South China Sea. *Geofluids*, 2019,  
1035 3240697. doi:10.1155/2019/3240697
- 1036 Di, P., Feng, D., Tao, J., & Chen, D. (2020). Using time-series videos to quantify methane  
1037 bubbles flux from natural cold seeps in the South China Sea. *Minerals*, 10(3), 216.  
1038 doi:10.3390/min10030216
- 1039 Dorman, C. E., & Winant, C. D. (2000). The structure and variability of the marine atmosphere  
1040 around the Santa Barbara Channel. *Monthly Weather Review*, 128(2), 261-282.  
1041 doi:10.1175/1520-0493(2000)128<0261
- 1042 Edinger, J. G. (1959). Changes in the depth of the marine layer over the Los Angeles Basin.  
1043 *Journal of Meteorology*, 16(3), 219-226. doi:10.1175/1520-  
1044 0469(1959)016<0219:citdot>2.0.co;2
- 1045 Etiopie, G., & Cicciooli, P. (2009). Earth's degassing: A missing ethane and propane source.  
1046 *Science*, 323(5913), 478-478. doi:10.1126/science.1165904

1047 Etiopé, G., Ciotoli, G., Schwietzke, S., & Schoell, M. (2019). Gridded maps of geological  
1048 methane emissions and their isotopic signature. *Earth System Science Data*, *11*(1), 1-22.  
1049 doi:10.5194/essd-11-1-2019

1050 Etiopé, G., & Schwietzke, S. (2019). Global geological methane emissions: An update of top-  
1051 down and bottom-up estimates. *Elementa: Science of the Anthropocene*, *7*.  
1052 doi:10.1525/elementa.383

1053 Fischer, P. J. (1978). Oil and Tar Seeps, Santa Barbara Basin, California. In D. J. Everitts, R. G.  
1054 Paul, C. F. Eaton, & E. E. Welday (Eds.), *California Offshore Gas, Oil and Tar Seeps*  
1055 (pp. 1-62). Sacramento, California: California State Lands Commission.

1056 Freeworldmaps (Cartographer). (2020). Physical Map of California. Retrieved from  
1057 <https://www.freeworldmaps.net/united-states/california/map.html>

1058 Frew, N. M., Bock, E. J., Schimpf, U., Hara, T., Haußecker, H., Edson, J. B., . . . Jähne, B.  
1059 (2004). Air-sea gas transfer: Its dependence on wind stress, small-scale roughness, and  
1060 surface films. *Journal of Geophysical Research: Oceans*, *109*(C8), C08S17.  
1061 doi:10.1029/2003JC002131

1062 Greinert, J. (2008). Monitoring temporal variability of bubble release at seeps: The  
1063 hydroacoustic swath system GasQuant. *Journal of Geophysical Research*, *113*, C07048.  
1064 doi:10.1029/2007JC004704

1065 Greinert, J., McGinnis, D. F., Naudts, L., Linke, P., & De Batist, M. (2010). Atmospheric  
1066 methane flux from bubbling seeps: Spatially extrapolated quantification from a Black Sea  
1067 shelf area. *Journal of Geophysical Research*, *115*. doi:10.1029/2009jc005381

1068 Hanna, S. R., Briggs, G. A., & Hosker Jr., R. P. (1982). *Handbook on Atmospheric Diffusion* (J.  
1069 S. Smith Ed.): Technical Information Center, U.S. Department of Energy.

1070 Helmig, D., Rossabi, S., Hueber, J., Tans, P., Montzka, S. A., Masarie, K., . . . Pozzer, A. (2016).  
1071 Reversal of global atmospheric ethane and propane trends largely due to US oil and  
1072 natural gas production. *Nature Geoscience*, *9*(7), 490-495. doi:10.1038/ngeo2721

1073 Heyer, J., & Berger, U. (2000). Methane emission from the coastal area in the Southern Baltic  
1074 Sea. *Estuarine, Coastal and Shelf Science*, *51*(1), 13-30. doi:10.1006/ecss.2000.0616

1075 Higgs, B., Mountjoy, J. J., Crutchley, G. J., Townend, J., Ladroit, Y., Greinert, J., & McGovern,  
1076 C. (2019). Seep-bubble characteristics and gas flow rates from a shallow-water, high-  
1077 density seep field on the shelf-to-slope transition of the Hikurangi subduction margin.  
1078 *Marine Geology*, *417*, 105985. doi:10.1016/j.margeo.2019.105985

1079 Hmiel, B., Petrenko, V. V., Dyonisius, M. N., Buizert, C., Smith, A. M., Place, P. F., . . .  
1080 Dlugokencky, E. (2020). Preindustrial 14CH<sub>4</sub> indicates greater anthropogenic fossil CH<sub>4</sub>  
1081 emissions. *Nature*, *578*(7795), 409-412. doi:10.1038/s41586-020-1991-8

1082 Höglund-Isaksson, L. (2017). Bottom-up simulations of methane and ethane emissions from  
1083 global oil and gas systems 1980 to 2012. *Environmental Research Letters*, *12*(2), 024007.  
1084 doi:10.1088/1748-9326/aa583e

1085 Hornafius, S. J., Quigley, D. C., & Luyendyk, B. P. (1999). The world's most spectacular marine  
1086 hydrocarbons seeps (Coal Oil Point, Santa Barbara Channel, California): Quantification  
1087 of emissions. *Journal Geophysical Research - Oceans*, *104*(C9), 20,703-720,711.  
1088 doi:10.1029/1999JC900148

1089 Hughes, M., Hall, A., & Fovell, R. G. (2007). Dynamical controls on the diurnal cycle of  
1090 temperature in complex topography. *Climate Dynamics*, *29*(2), 277-292.  
1091 doi:10.1007/s00382-007-0239-8

1092 IEA. (2020). *Methane Tracker 2020*. Retrieved from Paris: [https://www.iea.org/reports/methane-](https://www.iea.org/reports/methane-tracker-2020)  
1093 [tracker-2020](https://www.iea.org/reports/methane-tracker-2020)

1094 IPCC. (2013). *Working Group I Contribution to the IPCC Fifth Assessment Report Climate*  
1095 *Change 2013-The Physical Science Basis*. Retrieved from IPCC Secretariat, Geneva,  
1096 Switzerland:

1097 IPCC. (2014). *Climate Change 2014: Synthesis Report. Contributions of Working Groups I, II*  
1098 *and III to the Fifth Assessment Report of the Intergovernmental Panel on Climate*  
1099 *Change*. Retrieved from Geneva, Switzerland: [http://www.ipcc.ch/pdf/assessment-](http://www.ipcc.ch/pdf/assessment-report/ar5/syr/SYR_AR5_FINAL_full_wcover.pdf)  
1100 [report/ar5/syr/SYR\\_AR5\\_FINAL\\_full\\_wcover.pdf](http://www.ipcc.ch/pdf/assessment-report/ar5/syr/SYR_AR5_FINAL_full_wcover.pdf)

1101 Jackson, R. B., Saunio, M., Bousquet, P., Canadell, J. G., Poulter, B., Stavert, A. R., . . .  
1102 Tsuruta, A. (2020). Increasing anthropogenic methane emissions arise equally from  
1103 agricultural and fossil fuel sources. *Environmental Research Letters*, *15*(7), 071002.  
1104 doi:10.1088/1748-9326/ab9ed2

1105 Johansen, C., Macelloni, L., Natter, M., Silva, M., Woosley, M., Woolsey, A., . . . MacDonald, I.  
1106 R. (2020). Hydrocarbon migration pathway and methane budget for a Gulf of Mexico  
1107 natural seep site: Green Canyon 600. *Earth and Planetary Science Letters*, *545*, 116411.  
1108 doi:10.1016/j.epsl.2020.116411

1109 Johansen, C., Todd, A. C., & MacDonald, I. R. (2017). Time series video analysis of bubble  
1110 release processes at natural hydrocarbon seeps in the Northern Gulf of Mexico. *Marine*  
1111 *and Petroleum Geology*, *82*, 21-34. doi:10.1016/j.marpetgeo.2017.01.014

1112 Jordan, S. F. A., Treude, T., Leifer, I., Janßen, R., Werner, J., Schulz-Vogt, H., & Schmale, O.  
1113 (2020). Bubble-mediated transport of benthic microorganisms into the water column:  
1114 Identification of methanotrophs and implication of seepage intensity on transport  
1115 efficiency. *Scientific Reports*, *10*(1), 4682. doi:10.1038/s41598-020-61446-9

1116 Judd, A., & Hovland, M. (2007). *Seabed fluid flow: The impact on geology, biology and the*  
1117 *marine environment*. Cambridge, UK: Cambridge University Press.

1118 Kasaya, T., Mitsuzawa, K., Goto, T.-n., Iwase, R., Sayanagi, K., Araki, E., . . . Nagao, T. (2009).  
1119 Trial of multidisciplinary observation at an expandable sub-marine cabled station “Off-  
1120 Hatsushima Island Observatory” in Sagami Bay, Japan. *Sensors*, *9*(11), 9241-9254.  
1121 doi:10.3390/s91109241

1122 Leifer, I. (2010). Characteristics and scaling of bubble plumes from marine hydrocarbon seepage  
1123 in the Coal Oil Point seep field. *Journal Geophysical Research*, *115*(C11), C11014.  
1124 doi:10.1029/2009JC005844

1125 Leifer, I. (2015). Seabed bubble flux estimation by calibrated video survey for a large blowout  
1126 seep in the North Sea. *Journal of Marine and Petroleum Geology*, *68B*, 743-752.  
1127 doi:10.1016/j.marpetgeo.2015.08.032

1128 Leifer, I. (2019). A synthesis review of emissions and fates for the Coal Oil Point marine  
1129 hydrocarbon seep field and California marine seepage. *Geofluids*, *2019*(4724587), 1-48.  
1130 doi:10.1155/2019/4724587

1131 Leifer, I., & Boles, J. (2005). Turbine tent measurements of marine hydrocarbon seeps on  
1132 subhourly timescales. *Journal of Geophysical Research-Oceans*, *110*(C1), C01006.  
1133 doi:10.1029/2003jc002207

1134 Leifer, I., Boles, J. R., Luyendyk, B. P., & Clark, J. F. (2004). Transient discharges from marine  
1135 hydrocarbon seeps: Spatial and temporal variability. *Environmental Geology*, *46*(8),  
1136 1038-1052. doi:10.1007/s00254-004-1091-3

1137 Leifer, I., Chernykh, D., Shakhova, N., & Semiletov, I. (2017). Sonar gas flux estimation by  
1138 bubble insonification: Application to methane bubble flux from seep areas in the outer  
1139 Laptev Sea. *The Cryosphere*, 11(3), 1333-1350. doi:10.5194/tc-11-1333-2017

1140 Leifer, I., & Clark, J. F. (2002). Modeling trace gases in hydrocarbon seep bubbles: Application  
1141 to marine hydrocarbon seeps in the Santa Barbara Channel. *Geologiya I Geofizika*, 47(7),  
1142 572-579.

1143 Leifer, I., Clark, J. F., & Chen, R. F. (2000). Modifications of the local environment by natural  
1144 marine hydrocarbon seeps. *Geophysical Research Letters*, 27(22), 3711-3714.  
1145 doi:10.1029/2000GL011619

1146 Leifer, I., Jeuthe, H., Gjørund, S. H., & Johansen, V. (2009). Engineered and natural marine  
1147 seep, bubble-driven buoyancy flows. *Journal of Physical Oceanography*, 39(12), 3071-  
1148 3090. doi:10.1175/2009JPO4135.1

1149 Leifer, I., Kamerling, M., Luyendyk, B. P., & Wilson, D. (2010). Geologic control of natural  
1150 marine hydrocarbon seep emissions, Coal Oil Point seep field, California. *Geo-Marine  
1151 Letters*, 30(3-4), 331-338. doi:10.1007/s00367-010-0188-9

1152 Leifer, I., Luyendyk, B. P., Boles, J., & Clark, J. F. (2006). Natural marine seepage blowout:  
1153 Contribution to atmospheric methane. *Global Biogeochemical Cycles*, 20(3), GB3008.  
1154 doi:10.1029/2005GB002668

1155 Leifer, I., & MacDonald, I. (2003). Dynamics of the gas flux from shallow gas hydrate deposits:  
1156 interaction between oily hydrate bubbles and the oceanic environment. *Earth and  
1157 Planetary Science Letters*, 210(3-4), 411-424. doi:10.1016/S0012-821X(03)00173-0

1158 Leifer, I., Melton, C., Fischer, M. L., Fladeland, M., Frash, J., Gore, W., . . . Yates, E. L. (2018).  
1159 Atmospheric characterization through fused mobile airborne and surface in situ surveys:  
1160 Methane emissions quantification from a producing oil field. *Atmospheric Measurement  
1161 Techniques*, 11(3), 1689-1705. doi:10.5194/amt-11-1689-2018

1162 Leifer, I., Melton, C., Manish, G., & Leen, B. (2014). Mobile monitoring of methane leakage.  
1163 *Gases and Instrumentation*, July/August 2014, 20-24.

1164 Leifer, I., Melton, C., Tratt, D. M., Buckland, K. N., Chang, C., Frash, J., . . . Yurganov, L.  
1165 (2018). Validation of mobile in situ measurements of dairy husbandry emissions by  
1166 fusion of airborne/surface remote sensing with seasonal context from the Chino Dairy  
1167 Complex. *Environmental Pollution*, 242(Pt B), 2111-2134.  
1168 doi:10.1016/j.envpol.2018.03.078

1169 Leifer, I., Melton, C., Tratt, D. M., Buckland, K. N., Clarisse, L., Coheur, P., . . . Yurganov, L.  
1170 (2016). Remote sensing and in situ measurements of methane and ammonia emissions  
1171 from a megacity dairy complex: Chino, CA. *Environmental Pollution*, 221, 37-51.  
1172 doi:10.1016/j.envpol.2016.09.083

1173 Leifer, I., & Patro, R. (2002). The bubble mechanism for methane transport from the shallow  
1174 seabed to the surface: A review and sensitivity study. *Continental Shelf Research*, 22(16),  
1175 2409-2428. doi:10.1016/S0278-4343(02)00065-1

1176 Leifer, I., Solomon, E., Schneider v. Deimling, J., Coffin, R., Rehder, G., & Linke, P. (2015).  
1177 The fate of bubbles in a large, intense bubble plume for stratified and unstratified water:  
1178 Numerical simulations of 22/4b expedition field data. *Journal of Marine and Petroleum  
1179 Geology*, 68B, 806-823. doi:10.1016/j.marpetgeo.2015.07.025

1180 Liss, P. S., & Duce, R. A. (2005). *The sea surface and global change*: Cambridge University  
1181 Press.

1182 Liss, P. S., & Merlivat, L. (1986). Air-sea gas exchange rates: Introduction and synthesis. In P.  
1183 Buat-Ménard (Ed.), *The Role of Air-Sea Exchange in Geochemical Cycling* (Vol. 185).  
1184 Dordrecht: Springer.

1185 Lu, R., Turco, R. P., & Jacobson, M. Z. (1997). An integrated air pollution modeling system for  
1186 urban and regional scales: 1. Structure and performance. *Journal of Geophysical*  
1187 *Research: Atmospheres*, 102(D5), 6063-6079. doi:10.1029/96jd03501

1188 Marinaro, G., Etiope, G., Buc, N. L., Favali, P., Papatheodorou, G., Christodoulou, D., . . . Rolin,  
1189 J.-F. (2006). Monitoring of a methane-seeping pockmark by cabled benthic observatory  
1190 (Patras Gulf, Greece). *Geo-Marine Letters*, 26(5), 297-302. doi:10.1007/s00367-006-  
1191 0040-4

1192 Mazzini, A., Sciarra, A., Etiope, G., Sadavarte, P., Houweling, S., Pandey, S., & Husein, A.  
1193 (2021). Relevant methane emission to the atmosphere from a geological gas  
1194 manifestation. *Scientific Reports*, 11(1), 4138. doi:10.1038/s41598-021-83369-9

1195 Minor, S. A., Kellogg, K. S., Stanley, R. G., Gurrola, L. D., Keller, E. A., & Brandt, T. R.  
1196 (Cartographer). (2009). Geologic Map of the Santa Barbara Coastal Plain Area, Santa  
1197 Barbara County, California. Retrieved from <https://pubs.usgs.gov/sim/3001/>

1198 Münkel, C. (2007). Mixing height determination with lidar ceilometers - Results from Helsinki  
1199 Testbed. *Meteorologische Zeitschrift*, 16, 451-459. doi:10.1127/0941-2948/2007/0221

1200 Muyakshin, S. I., & Sauter, E. (2010). The hydroacoustic method for the quantification of the gas  
1201 flux from a submersed bubble plume. *Oceanology*, 50(6), 995-1001.  
1202 doi:10.1134/S0001437010060202

1203 Nicewonger, M. R., Verhulst, K. R., Aydin, M., & Saltzman, E. S. (2016). Preindustrial  
1204 atmospheric ethane levels inferred from polar ice cores: A constraint on the geologic  
1205 sources of atmospheric ethane and methane. *Geophysical Research Letters*, 43(1), 214-  
1206 221. doi:<https://doi.org/10.1002/2015GL066854>

1207 Nightingale, P. D., Malin, G., Law, C. S., Watson, A. J., Liss, P. S., Liddicoat, M. I., . . . Upstill-  
1208 Goddard, R. C. (2000). In situ evaluation of air-sea gas exchange parameterizations using  
1209 novel conservative and volatile tracers. *Global Biogeochemical Cycles*, 14(1), 373-387.  
1210 doi:10.1029/1999GB900091

1211 Nisbet, E. G., Manning, M. R., Dlugokencky, E. J., Fisher, R. E., Lowry, D., Michel, S. E., . . .  
1212 White, J. W. C. (2019). Very strong atmospheric methane growth in the 4 years 2014–  
1213 2017: Implications for the Paris Agreement. *Global Biogeochemical Cycles*, 33(3), 318-  
1214 342. doi:10.1029/2018GB006009

1215 Olson, D. J. (1983). *Surface and subsurface geology of the Santa Barbara Goleta Metropolitan*  
1216 *area, Santa Barbara County, California*. (MS). Oregon State University, Retrieved from  
1217 [https://ir.library.oregonstate.edu/concern/graduate\\_thesis\\_or\\_dissertations/v692tb957?loc](https://ir.library.oregonstate.edu/concern/graduate_thesis_or_dissertations/v692tb957?locale=it)  
1218 [ale=it](https://ir.library.oregonstate.edu/concern/graduate_thesis_or_dissertations/v692tb957?locale=it)

1219 Padilla, A. M., Loranger, S., Kinnaman, F. S., Valentine, D. L., & Weber, T. C. (2019). Modern  
1220 assessment of natural hydrocarbon gas flux at the Coal Oil Point seep field, Santa  
1221 Barbara, California. *Journal of Geophysical Research: Oceans*, 124(4), 2472-2484.  
1222 doi:10.1029/2018jc014573

1223 Peischl, J., Ryerson, T. B., Brioude, J., Aikin, K. C., Andrews, A. E., Atlas, E., . . . Parrish, D. D.  
1224 (2013). Quantifying sources of methane using light alkanes in the Los Angeles basin,  
1225 California. *Journal of Geophysical Research: Atmospheres*, 118(10), 4974-4990.  
1226 doi:10.1002/jgrd.50413

1227 Pozzer, A., Pollmann, J., Taraborrelli, D., Jöckel, P., Helmig, D., Tans, P., . . . Lelieveld, J.  
1228 (2010). Observed and simulated global distribution and budget of atmospheric  
1229 C<sub>2</sub>-C<sub>5</sub> alkanes. *Atmospheric Chemistry and Physics*, 10(9),  
1230 4403-4422. doi:10.5194/acp-10-4403-2010

1231 Rahn, D. A., Parish, T. R., & Leon, D. (2017). Synthesis of observations from the Precision  
1232 Atmospheric Marine Boundary Layer Experiment (PreAMBLE). *Monthly Weather*  
1233 *Review*, 145(6), 2325-2342. doi:10.1175/mwr-d-16-0373.1

1234 Reeburgh, W. S. (2007). Oceanic methane biogeochemistry. *Chemical Reviews*, 107(2), 486-513.  
1235 doi:10.1021/cr050362v

1236 Reeburgh, W. S., Ward, B. B., Whalen, S. C., Sandbeck, K. A., Kilpatrick, K. A., & Kerkhof, L.  
1237 J. (1991). Black Sea methane geochemistry. *Deep Sea Research Part A. Oceanographic*  
1238 *Research Papers*, 38, S1189-S1210. doi:10.1016/S0198-0149(10)80030-5

1239 Rehder, G., Keir, R. S., Suess, E., & Rhein, M. (1999). Methane in the Northern Atlantic  
1240 controlled by microbial oxidation and atmospheric history. *Geophysical Research*  
1241 *Letters*, 26(5), 587-590. doi:10.1029/1999GL900049

1242 Riedel, M., Scherwath, M., Römer, M., Veloso, M., Heesemann, M., & Spence, G. D. (2018).  
1243 Distributed natural gas venting offshore along the Cascadia margin. *Nature*  
1244 *Communications*, 9(1), 3264. doi:10.1038/s41467-018-05736-x

1245 Römer, M., Hsu, C.-W., Loher, M., MacDonald, I. R., dos Santos Ferreira, C., Pape, T., . . .  
1246 Sahling, H. (2019). Amount and fate of gas and oil discharged at 3400 m water depth  
1247 from a natural seep site in the Southern Gulf of Mexico. *Frontiers in Marine Science*,  
1248 6(700). doi:10.3389/fmars.2019.00700

1249 Römer, M., Riedel, M., Scherwath, M., Heesemann, M., & Spence, G. D. (2016). Tidally  
1250 controlled gas bubble emissions: A comprehensive study using long-term monitoring data  
1251 from the NEPTUNE cabled observatory offshore Vancouver Island. *Geochemistry,*  
1252 *Geophysics, Geosystems*, 17(9), 3797-3814. doi:10.1002/2016GC006528

1253 Römer, M., Sahling, H., Pape, T., Bohrmann, G., & Spieß, V. (2012). Quantification of gas  
1254 bubble emissions from submarine hydrocarbon seeps at the Makran continental margin  
1255 (offshore Pakistan). *Journal of Geophysical Research: Oceans*, 117(C10), C10015.  
1256 doi:10.1029/2011jc007424

1257 Römer, M., Wenau, S., Mau, S., Veloso, M., Greinert, J., Schlüter, M., & Bohrmann, G. (2017).  
1258 Assessing marine gas emission activity and contribution to the atmospheric methane  
1259 inventory: A multidisciplinary approach from the Dutch Dogger Bank seep area (North  
1260 Sea). *Geochemistry, Geophysics, Geosystems*, 18(7), 2617-2633.  
1261 doi:10.1002/2017gc006995

1262 Saunois, M., Stavert, A. R., Poulter, B., Bousquet, P., Canadell, J. G., Jackson, R. B., . . .  
1263 Zhuang, Q. (2020). The global methane budget 2000-2017. *Earth System Science Data*,  
1264 12(3), 1561-1623. doi:10.5194/essd-2019-128

1265 Sauter, E. J., Muyakshin, S. I., Charlou, J.-L., Schlüter, M., Boetius, A., Jerosch, K., . . . Klages,  
1266 M. (2006). Methane discharge from a deep-sea submarine mud volcano into the upper  
1267 water column by gas hydrate-coated methane bubbles. *Earth and Planetary Science*  
1268 *Letters*, 243(3-4), 354-365. doi:10.1016/j.epsl.2006.01.041

1269 Scherwath, M., Thomsen, L., Riedel, M., Römer, M., Chatzievangelou, D., Schwendner, J., . . .  
1270 Heesemann, M. (2019). Ocean observatories as a tool to advance gas hydrate research.  
1271 *Earth and Space Science*, 6(12), 2644-2652. doi:10.1029/2019ea000762

1272 Schmale, O., Beaubien, S. E., Rehder, G., Greinert, J., & Lonmbardi, S. (2010). Gas seepage in  
1273 the Dnepr paleo-delta area (NW-Black Sea) and its regional impact on the water column  
1274 methane cycle. *Journal of Marine Systems*, 80(1-2), 90-100.  
1275 doi:10.1016/j.jmarsys.2009.10.003

1276 Schmale, O., Greinert, J., & Rehder, G. (2005). Methane emission from high-intensity marine  
1277 gas seeps in the Black Sea into the atmosphere. *Geophysical Research Letters*, 32(7),  
1278 L07609. doi:10.1029/2004gl021138

1279 Schmale, O., Leifer, I., Stolle, C., Schneider von Deimling, J., Krause, S., Kießlich, K., . . .  
1280 Treude, T. (2015). Bubble transport mechanism: Indications for a gas bubble-mediated  
1281 inoculation of benthic methanotrophs into the water column. *Continental Shelf*  
1282 *Research*, 103, 70-78. doi:10.1016/j.csr.2015.04.022

1283 Schneider von Deimling, J., Rehder, G., Greinert, J., McGinnis, D. F., Boetius, A., & Linke, P.  
1284 (2011). Quantification of seep-related methane gas emissions at Tommeliten, North Sea.  
1285 *Continental Shelf Research*, 31, 867-878. doi:10.1016/j.csr.2011.02.012

1286 Schwietzke, S., Sherwood, O. A., Bruhwiler, L. M. P., Miller, J. B., Etiope, G., Dlugokencky, E.  
1287 J., . . . Tans, P. P. (2016). Upward revision of global fossil fuel methane emissions based  
1288 on isotope database. *Nature*, 538(7623), 88-91. doi:10.1038/nature19797

1289 Shakhova, N., Semiletov, I., Leifer, I., Rekant, P., Salyuk, A., & Kosmach, D. (2010).  
1290 Geochemical and geophysical evidence of methane release over the East Siberian Arctic  
1291 Shelf. *Journal of Geophysical Research*, 115(C8), C08007. doi:10.1029/2009JC005602

1292 Shakhova, N., Semiletov, I., Salyuk, A., Iossoupov, V., Kosmach, D., & Gustafsson, O. (2010).  
1293 Extensive methane venting to the atmosphere from sediments of the East Siberian Arctic  
1294 Shelf. *Science*, 327, 1246-1249. doi:10.1126/science.1182221

1295 Shakhova, N., Semiletov Igor P., Leifer, I., Sergienko, V., Salyuk, A., Kosmach, D., . . .  
1296 Gustafsson, O. (2013). Ebullition and storm-induced methane release from the East  
1297 Siberian Arctic Shelf. *Nature Geoscience*, 7, 64-70. doi:10.1038/ngeo2007

1298 Shindell, D. T., Faluvegi, G., Bell, N., & Schmidt, G. A. (2005). An emissions-based view of  
1299 climate forcing by methane and tropospheric ozone. *Geophysical Research Letters*, 32,  
1300 L04803. doi:10.1029/2004GL021900

1301 Simpson, I. J., Sulbaek Andersen, M. P., Meinardi, S., Bruhwiler, L., Blake, N. J., Helmig, D., . . .  
1302 . Blake, D. R. (2012). Long-term decline of global atmospheric ethane concentrations and  
1303 implications for methane. *Nature*, 488(7412), 490-494. doi:10.1038/nature11342

1304 Solomon, E., Kastner, M., MacDonald, I. R., & Leifer, I. (2009). Considerable methane fluxes to  
1305 the atmosphere from hydrocarbon seeps in the Gulf of Mexico. *Nature Geoscience*, 2,  
1306 561-565. doi:10.1038/NGEO574

1307 Thompson, D., Leifer, I., Bovensman, H., Eastwood, M., Fladeland, M., Frankenberg, C., . . .  
1308 Thorpe, A. K. (2015). Real-time remote detection and measurement for airborne imaging  
1309 spectroscopy: A case study with methane. *Atmospheric Measurement Techniques*, 8, 1-  
1310 46. doi:10.5194/amtd-8-1-2015

1311 Thornton, B. F., Prytherch, J., Andersson, K., Brooks, I. M., Salisbury, D., Tjernström, M., &  
1312 Crill, P. M. (2020). Shipborne eddy covariance observations of methane fluxes constrain  
1313 Arctic sea emissions. *Science Advances*, 6(5), eaay7934. doi:10.1126/sciadv.aay7934

1314 Veloso-Alarcón, M. E., Jansson, P., De Batist, M., Minshull, T. A., Westbrook, G. K., Pälke, H.,  
1315 . . . Greinert, J. (2019). Variability of acoustically evidenced methane bubble emissions  
1316 offshore Western Svalbard. *Geophysical Research Letters*, 46(15), 9072-9081.  
1317 doi:10.1029/2019gl082750



1318 Wanninkhof, R., Asher, W. E., Ho, D. T., Sweeney, C., & McGillis, W. R. (2009). Advances in  
1319 quantifying air-sea gas exchange and environmental forcing. *Annual Review of Marine*  
1320 *Science*, 1(1), 213-244. doi:10.1146/annurev.marine.010908.163742

1321 Washburn, L., Johnson, C., Gotschalk, C. G., & Eglund, E. T. (2001). A gas capture buoy for  
1322 measuring bubbling gas flux in oceans and lakes. *Journal of Atmospheric and Oceanic*  
1323 *Technology*, 18, 1411-1420. doi:10.1175/1520-0426

1324 Weber, D., Marquez, B. A., Taylor, C., Raya, P., Contreras, P., Howard, D., . . . Doezema, L. A.  
1325 (2017). Macroseepage of methane and light alkanes at the La Brea tar pits in Los  
1326 Angeles. *Journal of Atmospheric Chemistry*, 74(3), 339-356. doi:10.1007/s10874-016-  
1327 9346-4

1328 Weber, T. C., Mayer, L., Jerram, K., Beaudoin, J., Rzhanov, Y., & Lovalvo, D. (2014). Acoustic  
1329 estimates of methane gas flux from the seabed in a 6000 km<sup>2</sup> region in the Northern Gulf  
1330 of Mexico. *Geochemistry, Geophysics, Geosystems*, 15(5), 1911-1925.  
1331 doi:10.1002/2014gc005271

1332 Wiggins, S. M., Leifer, I., Linke, P., & Hildebrand, J. A. (2015). Long-term acoustic monitoring  
1333 at North Sea well site 22/4b. *Journal of Marine and Petroleum Geology*, 68, 776-788.  
1334 doi:10.1016/j.marpetgeo.2015.02.011

1335 Wilson, D., Leifer, I., & Maillard, E. (2015). Megaplume bubble process visualization by 3D  
1336 multibeam sonar mapping. *Journal of Marine and Petroleum Geology*, 68B, 753-765.  
1337 doi:10.1016/j.marpetgeo.2015.07.007

1338 Zhao, D., Toba, Y., Suzuki, Y., & Komori, S. (2003). Effect of wind waves on air-sea gas  
1339 exchange: Proposal of an overall CO<sub>2</sub> transfer velocity formula as a function of breaking-  
1340 wave parameter. *Tellus B: Chemical and Physical Meteorology*, 55(2), 478-487.  
1341 doi:10.3402/tellusb.v55i2.16747

1342 Zhao, Y., Saunois, M., Bousquet, P., Lin, X., Berchet, A., Hegglin, M. I., . . . Zheng, B. (2020).  
1343 Influences of hydroxyl radicals (OH) on top-down estimates of the global and regional  
1344 methane budgets. *Atmospheric Chemistry Physics*, 20(15), 9525-9546. doi:10.5194/acp-  
1345 20-9525-2020  
1346

1347 **Table of Nomenclature**

1348	NMHC	Non Methane Hydro Carbons
1349	O&G	Oil and Gas
1350	TC	Total Carbon
1351	THC	Total HydroCarbon
1352	WCS	West Campus Station
1353	$C_{ave}(\theta)$	Wind direction-resolved average concentration
1354	$C_{CH4}$	Methane concentration
1355	$C_{max}(\theta)$	Wind direction-resolved maximum concentration
1356	$C_{med}(\theta)$	Wind direction-resolved median concentration
1357	$C_{obs}$	WCS observed concentration
1358	$C_{seep}$	Concentration in seep directions
1359	$C'_{sim}$	WCS simulated concentration
1360	$u_{ave}(\theta)$	Wind direction-resolved average $u$
1361	$u_{max}(\theta)$	Wind direction-resolved maximum $u$
1362	$u_{med}(\theta)$	Wind direction-resolved median $u$
1363	$u_{seep}$	Wind speed in seep directions
1364	$BL$	Boundary layer height
1365	$C$	Concentration
1366	$C(t, \theta)$	Wind direction and time-resolved average concentration
1367	$C'$	Plume <del>concentration anomaly</del>
1368	$C_1-C_6$	<del>Concentrations, Methane to hexane</del>
1369	$E_A$	Atmospheric emissions
1370	$E_B$	Seabed (bottom) emissions
1371	$E_{i,j}$	Grid cell $i, j$ atmospheric emissions
1372	$E_W$	Emissions to the water column in the near field
1373	$i$	Grid cell easting index
1374	$j$	Grid cell northing index
1375	$K(r, \theta)$	Wind direction and distance-resolved correction function to emissions
1376	$K(\theta)$	Wind direction varying, distance correction function to emissions
1377	$r$	Distance from WCS to cell $i, j$
1378	$R$	Residual in $C'$ after Gaussian functional fit
1379	$R^2$	Correlation coefficient
1380	$t$	Time
1381	$u$	Wind speed
1382	$u(\theta)$	Wind direction-resolved wind speed
1383	$x, y$	Cartesian coordinate system in wind reference frame
1384	$Y$	Northing offset of WCS
1385	$\delta\theta$	Model wind direction angular resolution
1386	$\phi(u)$	Wind probability distribution
1387	$\phi(\theta, C)$	Wind direction and concentration-resolved probability distribution
1388	$\phi(\theta, u)$	Wind direction and wind speed-resolved probability distribution
1389	$\phi(\omega)$	Sonar return probability distribution
1390	$\phi_A(E_A)$	Normalized atmospheric emissions probability
1391	$\phi_s(\omega)$	Normalized sonar return probability distribution
1392	$\theta$	Wind direction
1393	$\omega$	Sonar return
1394	$\psi$	Wind veering
1395	$\zeta$	Relative inshore and offshore emissions
1396		

Deleted: (

Deleted: ) concentration

Deleted: concentrations

1400 **Table 1. Atmospheric plume composition and model atmospheric emissions.**

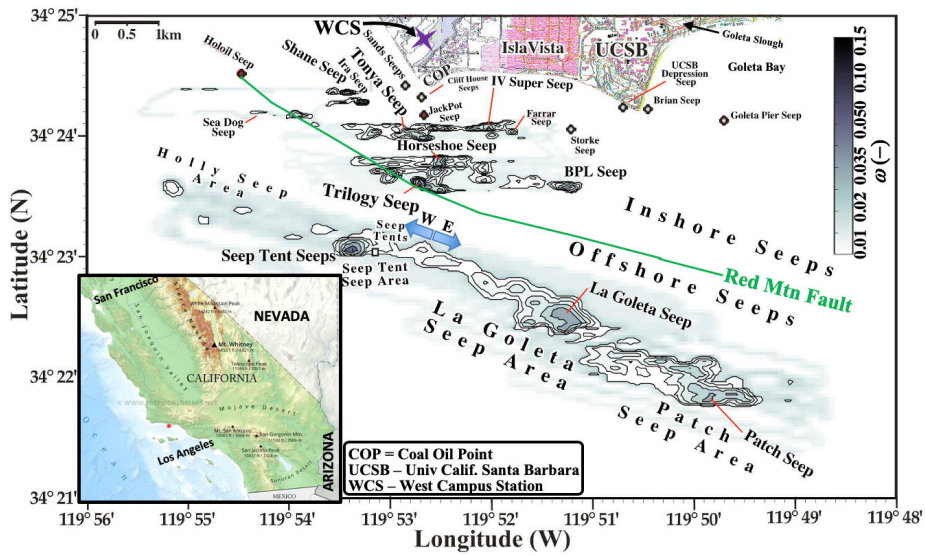
1401 Gas	<i>THC</i> Fraction	<i>TC</i> * Fraction	Emissions	Emissions
1402	(%)	(%)	(m <sup>3</sup> dy <sup>-1</sup> )	(Mg yr <sup>-1</sup> )
1403 CH <sub>4</sub>	88.5	72.8	73,900	19,300
1404 C <sub>2</sub> H <sub>6</sub>	3.10	2.55	2,590	1270
1405 C <sub>3</sub> H <sub>8</sub>	4.18	3.44	3,510	2520
1406 C <sub>4</sub> H <sub>10</sub>	2.76	2.27	2,300	2180
1407 C <sub>5</sub> H <sub>12</sub>	1.11	0.92	930	1090
1408 C <sub>6</sub> H <sub>14</sub>	0.133	0.11	110	150
1409 C <sub>6</sub> H <sub>6</sub>	7.8x10 <sup>-5</sup>	6.4x10 <sup>-5</sup>	7.1	8.3
1410 C <sub>7</sub> H <sub>16</sub>	0.036	0.030	29.7	45.8
1411 C <sub>7</sub> H <sub>8</sub>	1.8x10 <sup>-5</sup>	1.5x10 <sup>-5</sup>	1.8	2.3
1412 NMHC**	11.5	9.48	9,640	7410
1413 <i>THC</i> ***	85	82.3	83,400	26,600
1414 CO <sub>2</sub>		17.7	21,600	15200
1415 CO		0.003	3780	2660
1416				

1417 \**TC* is total carbon and is *THC*+CO+CO<sub>2</sub>

1418 \*\**NMHC* is non methane hydrocarbons and is C<sub>2</sub>-C<sub>7</sub>

1419 \*\*\**THC* is total hydrocarbon and is C<sub>1</sub>-C<sub>7</sub>

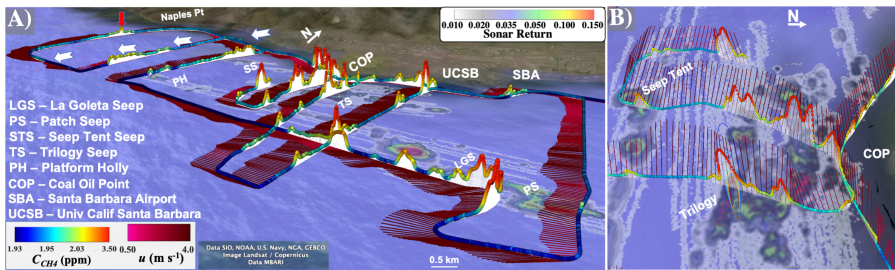
1420



1421 Figure 1: Sonar return,  $\omega$ , map after Leifer et al. (2010). Purple star marks West Campus Station, Seep area names are informal  
 1422 (Table S3), font size corresponds to strength. **W E** arrow segregates east and west offshore seepage. Data keys on panels. Inset  
 1423 shows S. California, red dot marks COP seep field. California inset map from Freeworldmaps (2020).  
 1424

- Deleted: (WCS)
- Deleted: E
- Deleted: W

1425



1429

1430

1431

1432

1433

1434

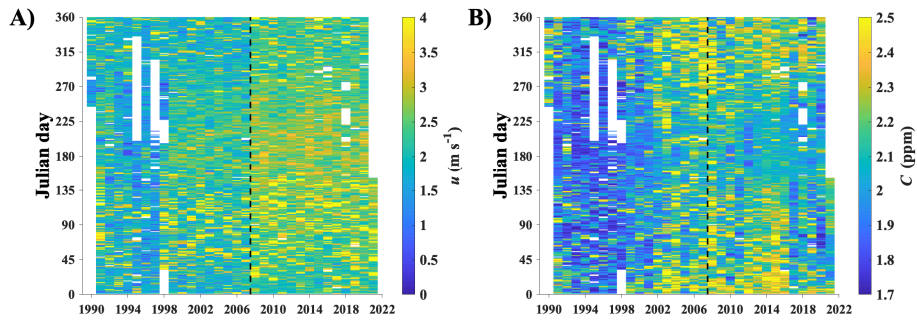
Figure 2: A) Methane,  $C_{CH_4}$ , and wind,  $u$ , data for 28 May 2016. White arrows show canyon offshore flow. Red arrows show unmapped seepage to the west of the COP seep field. B)  $C_{CH_4}$  and  $u$  showing Gaussian plume model for Trilogi Seep. Sonar return map shown on sea surface. Data key and seep name key on panel. Displayed in GoogleEarth. See Supp. Fig. S6 for overhead view.

1435

~~Deleted:~~ the

~~Deleted:~~ environment

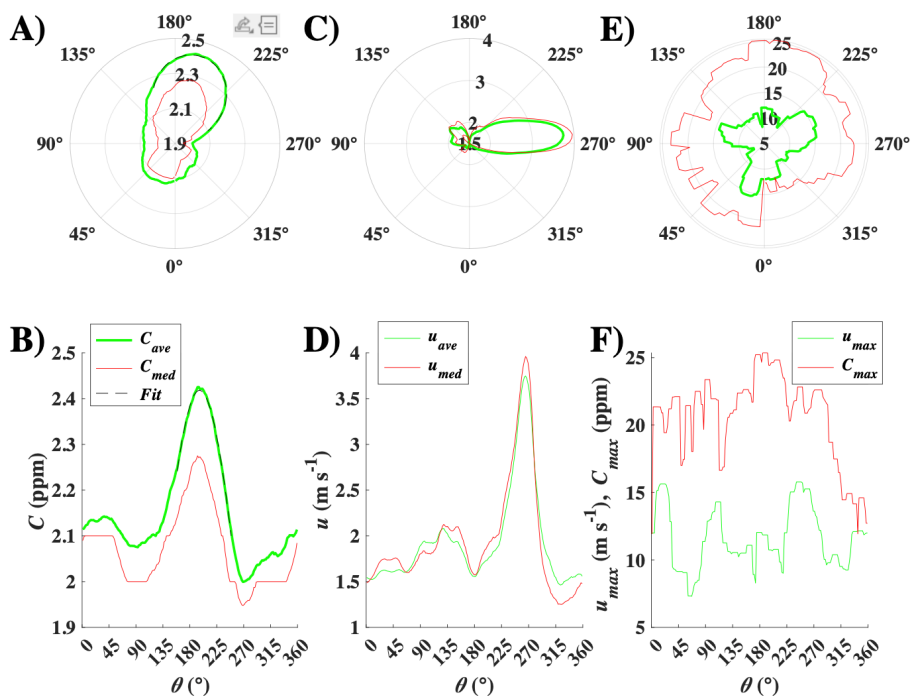
1438



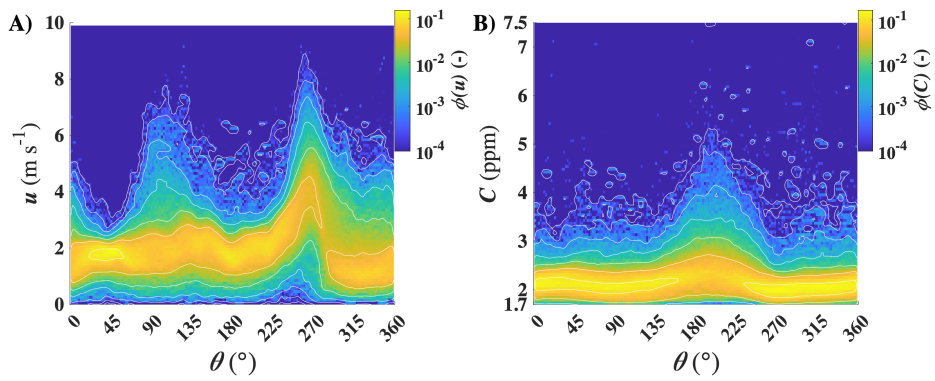
1439  
1440  
1441

Figure 3: A) Daily mean wind speed,  $u$ , and B) concentration,  $C$ . Data key on figure. WCS upgrade on Jan 2008 is shown by a dashed black line. Supp. Fig. S7 shows raw dataset.

1442



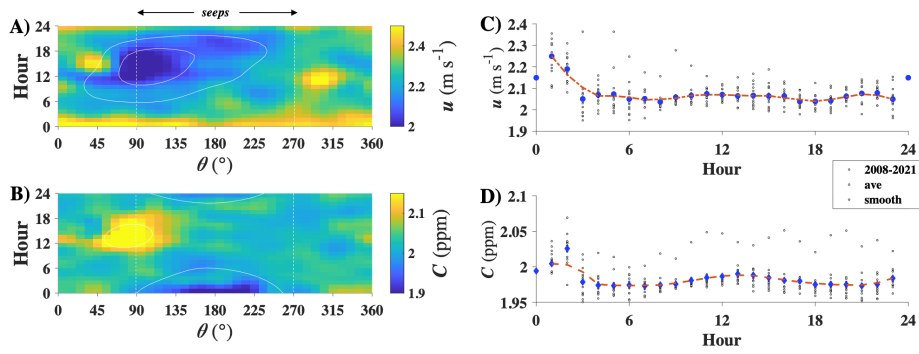
1444  
 1445 Figure 4: A, B) Concentration,  $C$ , versus wind-direction,  $\theta$ , 1990-2021 for average,  $C_{ave}(\theta)$ , and median,  $C_{med}(\theta)$ , and fit to  
 1446  $C_{ave}(\theta)$  for  $155 < \theta < 250^\circ$ . Data key on panel B. C, D) Wind speed,  $u$ , average,  $u_{ave}(\theta)$ , and median,  $u_{med}(\theta)$ . Data key on panel  
 1447 D. and E, F) Maximum  $C$ ,  $C_{max}(\theta)$ , and wind speed,  $u_{max}(\theta)$ . Data key on panel F. Polar plot oriented as at WCS facing the COP  
 1448 seep field.



1450  
 1451 Figure 5: A) Wind-direction,  $\theta$ , and wind-speed,  $u$ , resolved probability distribution,  $\phi(\theta, u)$  and B) Concentration probability  
 1452 distribution,  $\phi(\theta, C)$ , for 1990-2016. White dashed line shows edges of seep field. Data key on figure.  
 1453

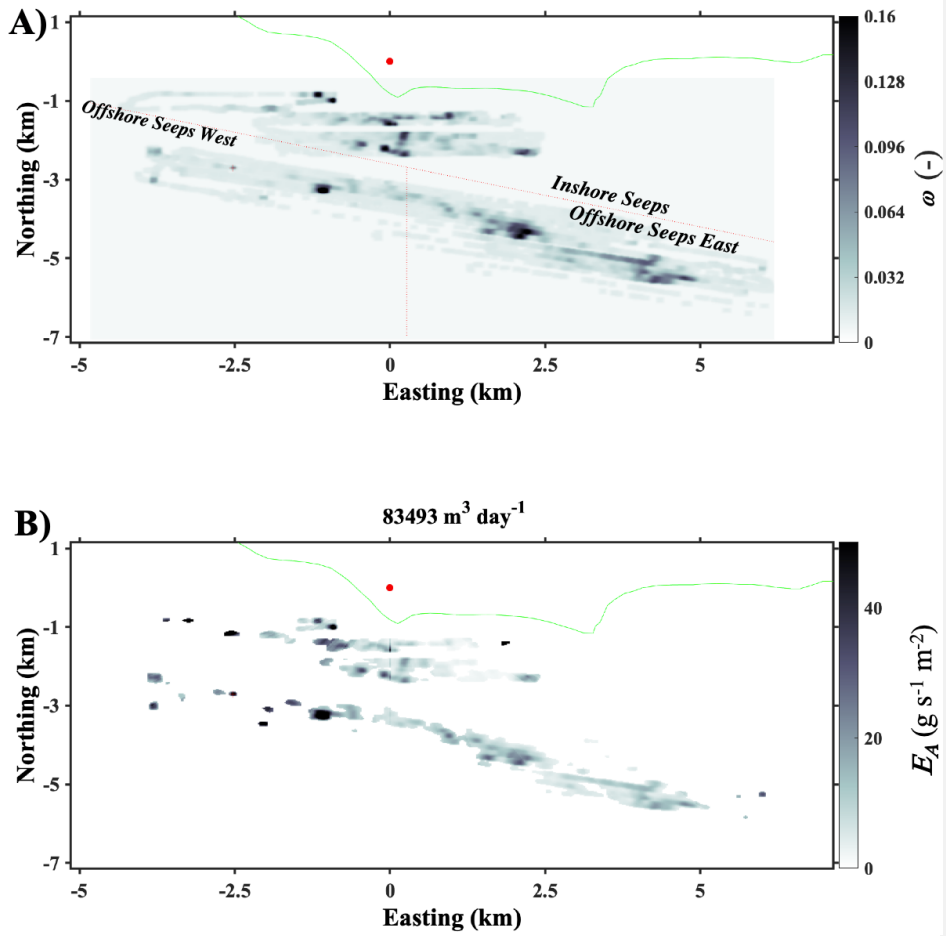


1454



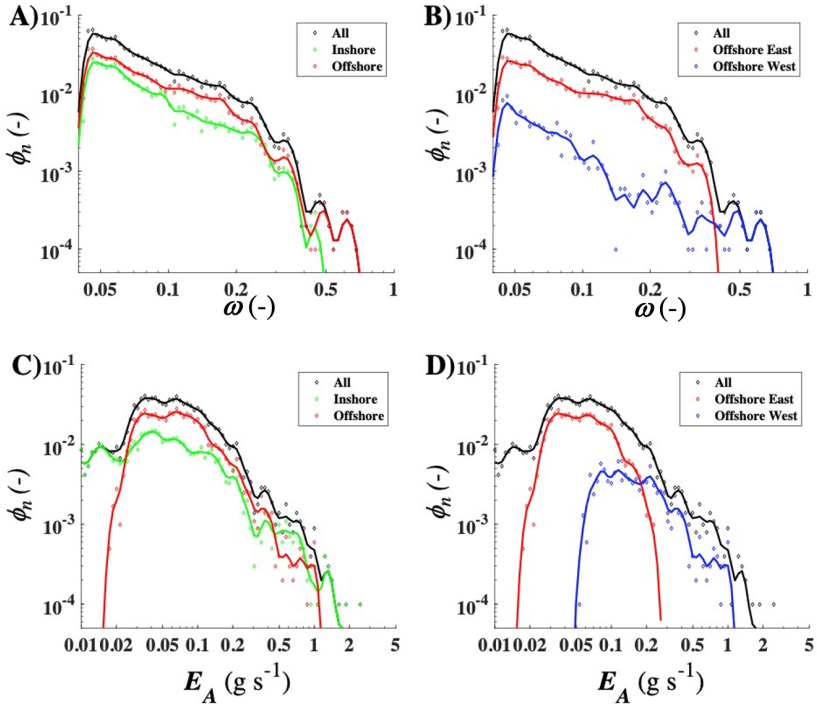
1455 Figure 6: A) 2008-2021 hour- and wind direction-,  $\theta$ , resolved wind speed,  $u$ , and B) concentration,  $C$ . C) Hourly-resolved, seep-  
1456 direction (90–270°), wind speed,  $u$ , and D) concentration,  $C$ , averaged, individual years, and 3-year smoothed. Data key on figure.  
1457  
1458 Midnight data missing due to daily calibration.

1459



1460 Figure 7: A) Sonar return,  $\omega$ , gridded at 22-m resolution. B) Atmospheric emissions,  $E_A$ . West campus station (red dot) is at  
 1461 coordinate system origin. Green line is coast line.  
 1462

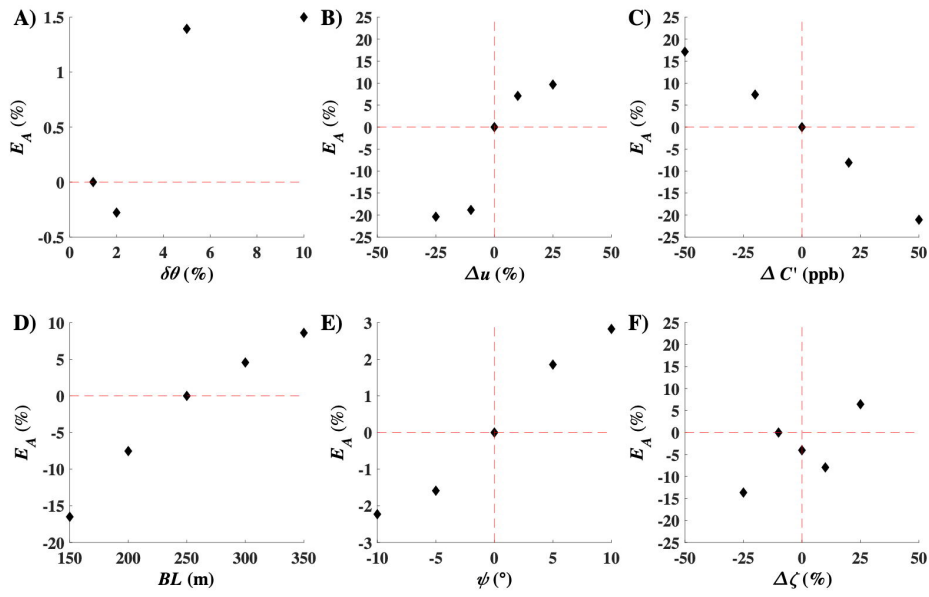
1463



1464  
 1465 Figure 8: A) Sonar return,  $\omega$ , occurrence probability,  $\phi_n(\omega)$ , for all seepage, inshore and offshore seepage and B) all seepage,  
 1466 offshore east seepage, and offshore west seepage. C) Atmospheric emission,  $E_A$ , occurrence probability,  $\phi_n(E_A)$ , for all seepage,  
 1467 inshore and offshore seepage and D) all seepage, offshore east seepage, and offshore west seepage. Data key on panels.

1468

1469



1470  
1471  
1472  
1473

Figure 9: Emissions,  $E_A$ , sensitivity to uncertainty in A) model angular resolution,  $\delta\theta$ , B) wind speed variation,  $\Delta u$ , C) concentration anomaly variation,  $\Delta C'$ , D) boundary layer thickness,  $BL$ , E) wind veering,  $\psi$ , and F) inshore/offshore partition variation,  $\Delta\zeta$ . Note different units on different plots. See text for details.



1474  
 1475  
 1476  
 1477

Figure 10: Map of the Goleta Plains oil and gas fields, wells, and the Coal Oil Point (COP) seep field. Grey hatch shows 1995 field extent, green outlines the 1940 field extent is from Leifer (2019). Field locations from Olson (1983). Well data from CDOGGR (2018). Faults from Minor et al. (2009). Seep names are informal. Data keys on panels. Shown in the © Google Earth environment.